ABSTRACT

SYNCHROTRON RADIATION-BASED CHARACTERIZATION OF GAN-BASED MQW STRUCTURES AND STRONGLY CORRELATED MATERIALS

by
Sean M. O'Malley

The following dissertation applies synchrotron radiation-based characterization techniques to the fields of gallium nitrides, multiferroic manganites, and self-assembled nano-domain oxide films. These material systems were chosen due to their unusual properties and potential device applications, which have made them very attractive to the scientific community.

Synchrotron-based High Resolution X-ray Diffraction (HRXRD) was used to characterize the structural properties of GaN-based multiple quantum well (MQW) structures grown on trapezoidal shaped GaN ridges. Results where interpreted within the framework of vapor-phase diffusion and surface-migration effects during the metalorganic vapor phase epitaxial growth. The relatively short diffusion length of group-III precursors and growth enhancement, due to facet migration was found to have significant effects on the MQW formation.

The use of synchrotron based HRXRD and in particular cross-sectional reciprocal space mapping (RSM) was then extended to studying the intriguing structural properties of a $ZnMnGaO_4$ film epitaxially grown on MgO (001) substrate. The results of this study helped in identifying the $ZnMnGaO_4$ film, as consisting of a self-assembled nano-checkerboard structure of highly aligned and regularly spaced vertical nanorods. The results demonstrated the importance of lattice distortion symmetry at the phase

boundaries as a means for the coherent coexistence of two domain types within the film volume.

Synchrotron-based far-infrared spectroscopy was performed at low temperatures on the single crystal multiferroic manganite $HoMn_2O_5$. A number of the infrared-active excitations were attributed to electric-dipole transitions between ligand-field split states of Ho^{3+} ions. It is proposed that the proximity in energy between magnons and Ho^{3+} ligand fields (LF) might connect the magnetism and dielectric properties of this compound through coupling with the Mn spin structure.

SYNCHROTRON RADIATION-BASED CHARACTERIZATION OF GaN-BASED MQW STRUCTURES AND STRONGLY CORRELATED MATERIALS

By
Sean M. O'Malley

A Dissertation
Submitted to the Faculty of
New Jersey Institute of Technology and
Rutgers, The State University of New Jersey-Newark
in Partial Fulfillment of the Requirements for the Degree of
Doctor of Philosophy in Applied Physics

Department of Applied Physics

January 2009

APPROVAL PAGE

SYNCHROTRON RADIATION-BASED CHARACTERIZATION OF GaN-BASED MQW STRUCTURES AND STRONGLY CORRELATED MATERIALS

Sean M. O'Malley

12/15/08

Dr. Andrei A. Sirenko, Dissertation Advisor — Date
Associate Professor of Applied Physics, NJIT

12/15/08

Dr. Daniel M. Bubb, Committee Member — Date
Associate Professor of Physics, Rutgers University-Camden

12/15/08

Dr. John F. Federici, Committee Member — Date
Professor of Applied Physics, NJIT

12/15/08

Dr. Leonid Tsybeskov, Committee Member — Date
Professor of Electrical and Computer Engineering, NJIT

12/15/08

Dr. Trevor A. Tyson, Committee Member — Date
Professor of Applied Physics, NJIT

12/15/08

Dr. Tao Zhou, Committee Member — Date
Assistant Professor of Applied Physics, NJIT

BIOGRAPHICAL SKETCH

Author: Sean M. O'Malley

Degree: Doctor of Philosophy

Date: January 2009

Undergraduate and Graduate Education:

- Doctor of Philosophy in Applied Physics,
  New Jersey Institute of Technology and Rutgers, The State University of New Jersey, Newark, NJ, 2009

- Bachelor of Science in Physics,
  Seton Hall University, South Orange, NJ, 2003

Major: Applied Physics

Publications and Presentations:

1. S. M. O'Malley, P. L. Bonanno, K. H. Ahn, and A. A. Sirenko, A. Kazimirov, S. Park and S-W. Cheong, "Epitaxial checkerboard arrangement of nanorods in ZnMnGaO4 films studied by x-ray diffraction", Phys. Rev. B **78**, 165424 (2008).

2. S. M. O'Malley, P. L. Bonanno, T. Wunderer, P. Brückner, B. Neubert, F. Scholz, A. Kazimirov, and A. A. Sirenko, "X-ray diffraction studies of selective area grown InGaN/GaN multiple quantum wells on multi-facet GaN ridges", phys. stat. sol. (c) **5**, 1655-1658 (2008).

3. A. A. Sirenko, S. M. O'Malley, and K. H. Ahn, S. Park, G. L. Carr, and S-W. Cheong, "Infrared-active excitations related to Ho^{3+} ligand-field splitting at the commensurate-incommensurate magnetic phase transition in $HoMn_2O_5$", Phys. Rev. B, **78**, 174405 (2008).

4. S. Gautier, T. Aggerstam, A. Pinos, S. Marcinkevicius, K. Liu, M. Shur, S. M. O'Malley, A. A. Sirenko, Z. Djebbour, A. Migan-Dubois, T. Moudakir, and A. Ougazzaden, "AlGaN/AlN multiple quantum wells grown by MOVPE on AlN templates using nitrogen as a carrier gas", Journal of Crystal Growth **310**, 4927 (2008).

5. P. L. Bonanno, S. M. O'Malley, A. A. Sirenko, A. Kazimirov, Z.-H. Cai, T. Wunderer, P. Brückner, and F. Scholz, "Intra-facet migration effects in InGaN/GaN MQW structures grown on triangular GaN ridges studied by submicron beam X-ray diffraction", Appl. Phys. Lett. **92**, 123106 (2008).

6. S. Park, Y. Horiba, T. Asada, L. S. Wielunski, N. lee, P. L. Bananno, S. M. O'Malley, A. A. Sirenko, A. Kazimirov, M. Tanimura, T. Gustafsson, and S.-W. Cheong, "Highly aligned epitaxial nanorods with a checkerboard pattern in oxide films", Nano Lett. **8**, 720 (2008).

7. A. A. Sirenko, A. Kazimirov, A. Ougazzaden, S. M. O'Malley, D. H. Bilderback, Z.-H. Cai, B. Lai, R. Huang, V. Gupta, M. Chien, S.N.G. Chu, "Surface migration effects in InGaAlAs and InGaAsP selective area grown optoelectronic waveguides studied by high resolution X-ray diffraction with 240 nm beam size", Appl. Phys. Lett. **88**, 081111 (2006).

8. A. A. Sirenko, A. Kazimirov, R. Huang, D. H. Bilderback, S. M. O'Malley, V. Gupta, K. Bacher, L.J.P. Ketelsen, and A. Ougazzaden, "Micro-beam high-resolution x-ray diffraction in strained InGaAlAs-based multiple quantum well laser structures grown selectively on masked InP substrates", Journal of Applied Physics, **97**, 063512 (2005).

9. A. Ougazzaden, S. M. O'Malley, A. A. Sirenko, A. Kazimirov, R. Huang, D. H. Bilderback, V. Gupta, K. Bacher, and L.J.P. Ketelsen, "Deep analysis of Selective area growth InGaAlAs SAG MQWs structures using micro beam high resolution X-ray diffraction and micro photoluminescence", Proceedings of the 11th European Workshop on MOVPE, Lausanne June 5th-8th (2005), pp. 127-128 (B03).

10. D. M. Bubb, S. M. O'Malley, C. Antonacci, R. Belmont, R. A. McGill, and C. Crimi, "Observation of Persistent Photoconductivity in Conducting Polyaniline Thin Films", Applied Physics A **81**, 119-25 (2005).

11. C. Toftmann, M. R. Papantonakis, R. C. Y. Auyeung, W. Kim, S. M. O'Malley, D. M. Bubb, J. S. Horwitz, J. Schou, P. M. Johansen, and R. F. Haglund, "UV and RIR matrix assisted pulsed laser deposition of organic MEH-PPV films", Thin Solid Films **453**, 177 (2004).

12. D. M. Bubb, S. M. O'Malley, C. Antonacci, D. Simonson, and R. A. McGill, "Matrix-Assisted Laser Deposition of a Sorbent Chemoselective Oligimer Using an Infrared Laser", Journal of Applied Physics **95**, 2175 (2004).

Invited Talks:

1. GK-12 Teacher Professional Development Workshops, "The Scientific Method with Microsoft Excel: Instilling Data Analysis Techniques", May (2008).

2. Cornell High Energy Synchrotron Source (CHESS) Graduate Student Symposium, "Growth Kinetics and Structural Properties of InGaN/GaN MWQ Studied by Synchrotron-Based X-Ray Diffraction", February (2008).

Posters:

1. Cornell High Energy Synchrotron Source (CHESS) User Meeting, Ithaca NY, June (2008).

2. Fourth Annual NJIT Provost's Student Research Showcase, Newark NJ, April (2008).

3. Eighth Annual NSF GK-12 Conference, Washington DC, February (2008).

4. Seventh Annual International Conference of Nitride Semiconductors, Las Vegas, NV, September (2007).

To my beautiful wife, Anna
and our supportive families

ACKNOWLEDGMENT

I would like to thank my advisor Dr. Andrei Sirenko for the guidance and support he has given me in all aspects of my graduate work. I thoroughly enjoyed our conversations together and the insight and knowledge he has passed on to me, it was an indispensable part of my success. For this and many other deeds I am forever in his debt.

A special thanks goes to my Committee members: Dr. Daniel Bubb, Dr. John Federici, Dr. Leonid Tsybeskov, Dr. Trevor Tyson, and Dr. Tao Zhou. Dr. Bubb was my advisor at Seton Hall and the first person who introduced me to the wonderful world of experimental physics. I must also acknowledge the support from Dr. Federici and his postdoc, Lim. I could always count on Dr. Federici and his postdoc, Lim to kindly provide that soldering iron or whatever I happened to need for my experimental setup. Also, thanks go to Dr. Tsybeskov, Dr. Tyson and his graduate student, Peng Gao, for generously providing LN2 and support. I would also like to thank Dr. Tao for our exciting collaboration together during the summer of 2008.

I would like to also thank my friend and fellow student, Peter Bonanno. We spent many long hours together by the beamline collecting data and discussing results.

I am very grateful to Dr. Ken Ahn for his help with the theoretical aspects.

I am very grateful for the help and support of Dr. Alex Kazimirov (CHESS), Dr. Larry Carr (NSLS-BNL) and Dr. Zhonghou Cai (Advanced Photon Source). And a special thank you goes to the research groups of Dr. S-W Cheong (Rutgers University) and Dr. F. Scholz (Ulm of University, Germany) for providing the samples.

And, finally to my supportive family for their constant love, support and prayers.

Deo gratias.

TABLE OF CONTENTS

TABLE OF CONTENTS
(Continued)

TABLE OF CONTENTS
(Continued)

Chapter **Page**

LIST OF TABLES

LIST OF FIGURES

LIST OF FIGURES
(Continued)

LIST OF FIGURES
(Continued)

LIST OF FIGURES
(Continued)

LIST OF FIGURES
(Continued)

LIST OF FIGURES
(Continued)

LIST OF FIGURES
(Continued)

LIST OF FIGURES
(Continued)

Figure **Page**

CHAPTER 1

INTRODUCTION

Chapter 1 introduces the benefits of synchrotron radiation and provides background information on the three material systems that will be characterized using synchrotron radiation. These materials have attracted great interest within the scientific community due to their unusual properties and potential device applications.

1.1 Synchrotron Light Sources

The high intensity of synchrotron radiation means that x-ray beams can now be focused down to record small sizes, while it still retains reasonably large flux densities [1]. Combining this attribute with high resolution x-ray diffraction (HRXRD), a very important nondestructive characterization tool in the field of semiconductor physics, will allow for microbeam-HRXRD. The spatial resolution of micro-beam HRXRD can probe local structural quality in narrow regions of device structures. Therefore, this technique can be used to characterize semiconductor device structures with narrow in-plane widths (< 10 μm). The high intensity of synchrotron radiation in the far-infrared (FIR) is also a valuable asset in the study of a broad class of multiferroic crystals. The otherwise lengthy nature of FIR spectroscopy measurements of multiferroic crystals with their multiple parameters (temperature T, magnetic field H, and polarization P) and small crystal sizes can be considerably reduced. The spectral region for optically active phonons and magnons, most important to studies of the magnetoelectric effect, typically lay below 200

cm^{-1} where synchrotron-based FIR spectroscopy has an advantage with its extended spectral range extending down to only a few wavenumbers.

1.2 Group-III Nitride Semiconductors

Group-III nitrides have attracted great interest in the semiconductor community due to their application in short-wavelength light emitting devices and high power field effect transistors. AlN, GaN, InN and their corresponding alloys can, through bandgap engineering, produce light ranging from 200 to 656 nm [2], a range otherwise inaccessible with traditional III-V semiconductors such as GaAs and InP [3]. The realization of GaN-based devices was initially hindered by a lack of suitable substrates for epitaxial growth of optoelectronic device structures. Bulk GaN single crystals are still too expensive for commercial use; therefore, all growth needs to be heteroepitaxial [4]. GaN has a high melting temperature and very high decomposition pressure; therefore, it cannot be grown in commercial volumes using conventional methods e.g., Czochraslski or Bridgman growth [4]. Further complicating matters, GaN crystallizes in a hexagonal lattice that prohibits the utilization of commonly used cubic substrates like Si, InP and GaAs. Currently, the two most used substrates for heteroepitaxial growth of GaN are sapphire (Al_2O_3) and silicon-carbide (SiC); however, both have a large lattice mismatch with GaN of 16 % and 3.5 % respectively. The mismatch initiates formation of structural defects, the most prevalent being threading dislocations (TD). Dislocation densities on the order of 10^9 to 10^{10} cm^{-2} are typical of GaN grown layers, some six orders of magnitude greater than those found in GaAs grown layers [4]. Threading dislocations in optoelectronic devices have a negative impact on the quantum efficiently and lifetime of

the device, driving the efforts to improve structural quality of GaN epitaxial growth. The growth technique based on introduction of a specialized buffer layer is called epitaxial-lateral-overgrowth (ELOG). It has been successful in reducing TDs in GaN epilayers to a more reasonable density of ~10^7 cm^{-2} and therefore, helped improve device lifetimes to > 10,000 hrs [5].

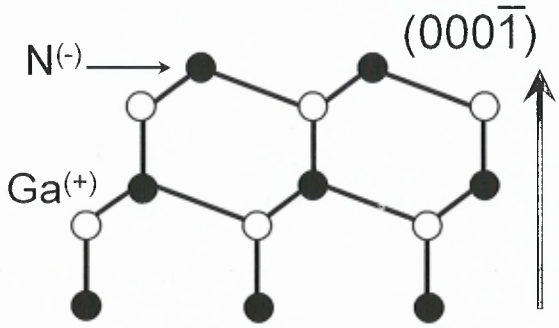

Figure 1.1 Illustration of the highly polar nature of the GaN wurtzite structure.

Though great strides have been made in GaN device growth recently, problems still exist for "longer" wavelength (λ > 500 nm) devices with Indium concentrations >10 % [6]. The incorporation of Indium in GaN is hindered by a miscibility gap between InN and GaN, due to the low binding energy between InN and GaN, and the large vapor pressure of nitrogen [7]. Large piezoelectric fields within the QW, due to highly polar nature of the GaN wurtize lattice along the c-axis, reduces the optical efficiency of devices. Figure 1.1 illustrates the polar nature of the wurtzite lattice with the alternating formation of Ga^+ and N^- ions along the <0001> direction. The effect is enhanced by the considerable lattice mismatch (~11%) between the InN and GaN constituents, generating a large c-axis strain [8]. The piezoelectric fields create a quantum confined Stark effect (QCSE) in the active MQW layers, reducing electron-hole recombination and redshifts

the transition energies [9]. One-way around this problem is to grow the QW on semi-polar planes, e.g., the *r*-plane, instead of the commonly used *c*-plane [10,11,12].

1.3 Multiferroic Materials

The field of multiferroics is comprised of a class of materials that exhibits, within the same phase, two or more primary ferroic-type behavior, e.g., ferroelectricity and antiferromagnetism [13]. In certain multiferroics, a strong interplay between the electric and magnetic properties exists such that the application of an external field or the onset of a phase transition in one category will change the properties of the other [14,15]. This profound interplay is known as the magnetoelectric effect, where the application of a magnetic field H may change the polarization P and/or dielectric constant ε. Though the magnetoelectric effect has been known for over hundred years, at least theoretically, interest in it didn't peak until the early 1970's. By the end of that decade, the number of publications dwindled, due to the general weakness of the effect in available compound at that time [16]. However, a recent revival fueled by the discovery of new compounds which display stronger magnetoelectric effects, like gigantic magnetocapacitance (GMC) in $TbMnO_3$ [14] and colossal magnetodielectric (CMD) effects in $DyMn_2O_5$ [15], has sparked renewed interest. These two magnetoelectric multiferroics comprise a class of rare earth manganese oxides $RMnO_3$ and RMn_2O_5, with rare earth elements from the middle of the lanthanide group. This interplay between electrical and magnetic properties has inspired many novel device designs [17]. In a 1970's review, by Wood and Austin, they listed some 15 different possible applications for multiferroic materials, included were ideas for optical switches, controlled by magnetically switching the polarization,

and the possibility of a memory-storage-device, whereby information could be written magnetically and read optically [18]. However, today their real use is still limited to the study of strongly correlated materials involving orbitals of *d* and *f* electrons, and these materials serve only as a benchmark for new theoretical and computational techniques [19].

1.4 Self-Assembled Nano-Domains

Consumer demand for faster and smaller electronic devices and manufactures willingness to accommodate these requests has fueled research and development towards exploration in nanotechnology. Whereby, reducing the physical device size whether it be the use of quantum-dot transistors in CPU applications or magnetic domains in magnetic hard drives to increase data storage has proven to be advantageous for improving electronic devices. The key towards achieving success in the nano-world however, is the ability to control the formation of nano-domains allowing for monolithic integration and increase device densities. This need for better spatial control during growth has peeked interest in growth techniques which are not restricted by spatial resolution, e.g., lithography, where even the best e-beam lithography methods are limited to tens of nanometers in size and require a number of post-possessing steps. This has leaded the scientific community to probe other avenues for device growth, such as those based on self-assembly, also known as self-organization.

The otherwise forgotten ternary oxide system of $ZnMnGaO_4$ (ZMGO) was recently discovered to undergo self-assembly into a checkerboard (CB) arrangement of compositionally and structurally different nano-rod regions. The compound crystallizes

into a spinel (XY_2O_4) structure, which ideally contains X cations at the tetrahedral (X) and octahedral (Y) lattice sites. During solid-phase growth, Mn^{3+} ions located at the octahedral sites can undergo Jahn-Teller (JT) distortions within the system, which the system harnesses to eventually form the nano-scale checkerboard structure.

The discovery of several material systems with periodic self-assembled nano-checkerboard (CB) structures [20,21,22,23,24,25,26] has shown potential for practical applications. Synthesis of spinel oxides with CB structures, such as nonmagnetic $ZnMnGaO_4$ (ZMGO) [20] and magnetic Mn-doped $CoFe_2O_4$ [23], relies on harnessing Jahn-Teller (JT) distortions in the solid-phase during growth to ultimately form nano-scale domain structures. For the purpose of device fabrication these novel nano-scale structures should be producible in the form of thin-films, which are compatible with general approaches of planar technology. In thin films, the material properties can be enhanced by an overall reduction in volume allowing for further monolithic integration of device components.

CHAPTER 2

EXPERIMENT METHODS

The following chapter provides background information on the experiential methods used in this dissertation and should act as a reference point for the reader.

2.1 High Resolution X-Ray Diffraction

High resolution x-ray diffraction (HRXRD) is a powerful nondestructive tool for the characterization of layered growth structures where knowledge of the structural parameters of the epilayer are of critical importance. The measured diffraction curves can provide detailed information on the thickness, strain, and composition along with a host of other structural parameters of the growth layer under investigation. Figure 2.1 depicts a simulated θ-2θ diffraction curve for an ideal InGaN/GaN MQW structure grown on *c*-axis GaN, where θ and 2θ are the angles of rotation of the sample and detector arm, respectively. This diffraction curve is representative of a typical scan along the growth direction in reciprocal space for layered heterostructures, containing a strong substrate peak with a number of weaker interference peaks associated with scattering from the alternating layer structure. The angular position of the substrate peak is governed by the famous Bragg law which states that scattering of x-rays from crystallographic planes interferes constructively for the following condition:

$$2d_{hkl}\sin\theta_{Bragg} = n\lambda, \tag{2.1}$$

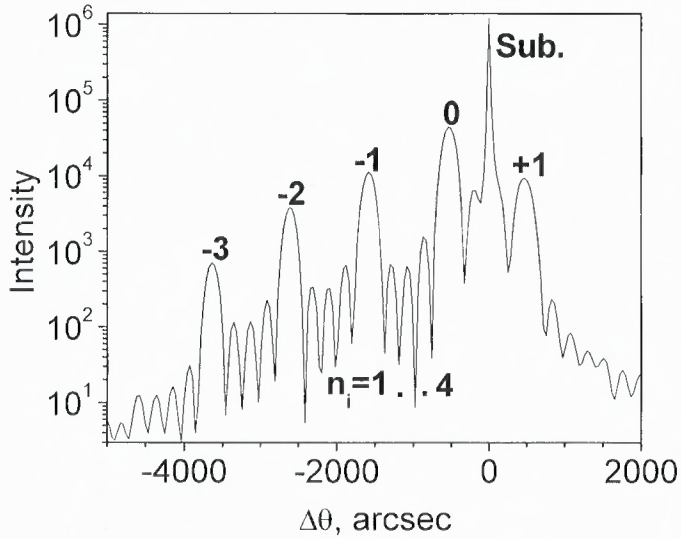

Figure 2.1 Simulated θ-2θ diffraction curve for the (00.2) reflection from five InGaN/GaN MQW growth on a GaN substrate. Well and barrier thickness was 40 and 80 nm respectively, with 20% Indium composition for the InGaN wells. The horizontal axis is in relative angular units (Δθ, arcsec) with respect to the GaN substrate peak θ_{Bragg}.

where d_{hkl} is the interplanar spacing, n is the order of diffraction, and λ is the wavelength of the incident x-ray beam. In the case of a symmetric θ-2θ scan, the reflection coincides with the planar surface of the substrate and is, therefore, only sensitive to planar separation parallel to the growth direction. For c-axis GaN this is the (0001) basal-plane. If information on in-plane lattice parameters are required, an asymmetric reflection needs to be used, which corresponds to a set of planes with a nonzero interplanar angle between the reflection and surface planes. When a heteroepitaxial layer is elastically grown on a substrate, the in-plane lattice constants of the layer are distorted to match that of the substrate (i.e., $a_{\parallel}^{L} = a_{\parallel}^{S}$). Assuming tetragonal distortion and no relaxation, the in-plane distortion results in a strain along the growth direction $S_{\perp}$, which can be directly

measured by the angular separation $\Delta\theta$ between the layer and substrate peaks, by the following expression [27]:

$$S_{\perp} = \frac{\Delta d}{d_s} = \Delta\theta \cot\theta_B, \tag{2.2}$$

Referring back to Figure 2.1, $\Delta\theta$ would correspond to the separation between the 0th order MQW satellite peak and the substrate peak. There are exceptions to the use of Equation 2.2 when the layer thickness become very small; in such a case appropriate modeling methods must be used to actually determine the strain value [28].

When a thin hetero-epilayer is grown, Pendellösung fringe peaks arise from interference effects between incident and scattered waves. In multilayered structures, further modulation will occur if the scattering form factors between the layers differ, as in the case of superlattices SL or MQW structures [29]. This further modulation, as seen in Figure 1.2, can then be used to determine the period and global strain of multilayered structure. The peaks arising from this modulation are commonly known as SL and/or MQW satellite peaks. The angular separation $\Delta\theta$ of the zeroth-order MQW peak from the substrate represents the "composite" strain S_{MQW} of the active region and is determined by:

$$S_{MQW} = \frac{\left(W_W \cdot S_W + W_B \cdot S_B\right)}{W_W + W_B}, \tag{2.3}$$

where $W_{W(B)}$ and $S_{W(B)}$ are the thickness and strain of the well (barrier), respectively [30]. The relative intensities of the SL satellite peaks are directly related to the $W_{W(B)}$, however, they are best determined through simulation software employing the Takagi-Taupin formalism, which can calculate dynamic scattering effects in high resolution diffraction.

The angular position of the adjacent MQW satellite peaks L_i and L_j, gives the QW period (P_{MQW}) through the relation: [29]

$$P = W_W + W_B = \frac{\left(L_i - L_j\right)\lambda}{2\left(\sin\theta_i - \sin\theta_j\right)}. \tag{2.4}$$

The number of quantum wells (N) can be determined by the number of subsidiary fringes between the MQW satellite peaks, where the number of fringe minima equals $N-1$, and the minima are known as Kiessig fringes. This data analysis approach is utilized in Chapters 4 and 6.

2.2 Reciprocal Space Mapping

HRXRD can be extended towards the measuring of reciprocal space maps (RSM) whereby a series of adjacent diffraction curves are collected and stitched together to form a map around a particular reciprocal lattice point (RLP). The technique is typically used to study mosaic spread and relaxation effects within the layers, but can also be extended to the determination of coherence length (e.g., grain size) and structural distortions such as tilt and twisting of the unit cell. This is possible by decoupling of the peak breadth into reflection-order dependent and independent components, for at least two reflections belonging to the same family of crystallographic planes. This dependence for peak breadth is described in the so-called Williamson-Hall model [31]. Figure 2.2 demonstrates the case where the peak breadth is a combination of an order independent lateral coherence length component and an order dependent tilt misorientation component. The dominance of either lateral grain size and/or tilt effects can be inspected visually in asymmetric RSM. The effect on tilt variation on the peak breadth is to rotate

the peak as shown by the asymmetric RPL in Figure 2.2. In contrast, lateral size dominance manifests itself as a broadening parallel to the sample surface [32]. We will use this approach for data analysis in Chapter 6.

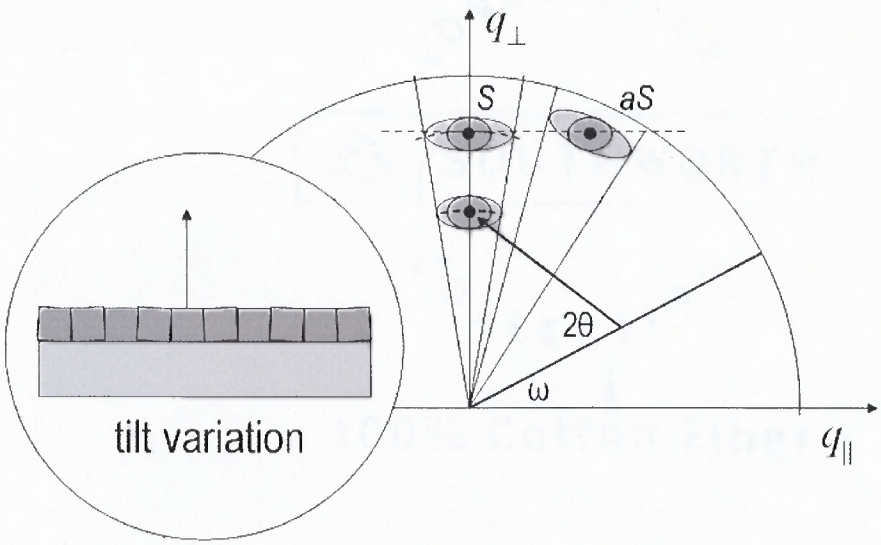

Figure 2.2 Illustration of lateral correlation length (dark gray) and tilt variation (light gray) contributions to the peak breadth for symmetric (S) and asymmetric (aS) reflections. Note that the tilt contribution is reflection-order-dependent while the coherence length contribution is independent of the reflection order.

Mapping in reciprocal space also be can be helpful in identifying the prevalence of dislocation types within the epitaxial layer. For instance, threading dislocations (TD) come in three major categories: screw, edge and mixed; all of which can cause a broadening of the mosaic spread by creating tilts, twists and a loss in the long-range coherence length of the lattice [33,34]. All reflections, both symmetric and asymmetric, with L nonzero are sensitive to screw TD along the [0001] direction. Edge TDs are located in planes with H or K nonzero; therefore, they can only be probed by asymmetric scans [35]. These dislocations cause distortions in the planes that cause a broadening in

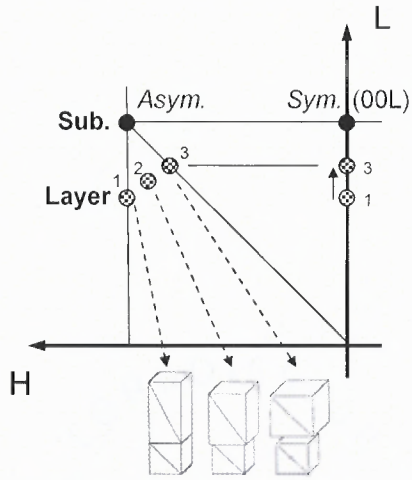

Figure 2.3 Schematic illustrating the effects of strain relaxation on the position of the epilayer peak in a reciprocal space map, for a symmetric (sym.) and asymmetric (asym.) reflections. Note this case has been generalized for cubic lattice.

the profile of the rocking-curves, where broadening in the θ-2θ curves are caused by thickness and compositional variations.

Asymmetric RSMs are particularly useful for the determination of layer quality because they are sensitive to parallel as well as perpendicular components of the lattice constants; thereby, providing information on the relaxation states of the grown layers. Equation 2.5 represents the state of relaxation (R), ranging from $R = 0$ (elastic strained) to 1 (completely relaxed), where $a_{\parallel}^{L}$ is the measured lattice parameter parallel to the surface, a_0^L and a_o^S are the intrinsic parallel lattice constant of the layer and substrate, respectively [36].

$$R = \frac{a_{\parallel}^{L} - a_0^S}{a_0^L - a_0^S} \tag{2.5}$$

In an elastically strained layer, the layer peak lays along a line parallel to the growth direction, as demonstrated in Figure 2.3 by layer peak position "1". As the layer progressively becomes more relaxed the asymmetric layer peak will shift, as depicted in

Figure 2.3, from position "1" to position "3". The corresponding shift for a symmetric reflection is strictly vertical and can not be decoupled from compositional changes in the layer [37]. The above approaches are used for data analysis in Chapters 4 and 6.

2.3 Far-Infrared Spectroscopy

Far-infrared Fourier Transform (FTIR) spectroscopy is a nondestructive optical characterization technique which can provide valuable information on the allowed dipole excitations. In the case of the multiferroic compounds this work is concerned with the existence of three primary excitations which may be present in the FTIR spectra: (I) phonons due to the collective excitation of lattice vibrations, (II) magnons from the propagation of spin waves in magnetically ordered phases, and (III) electronic dipole transitions from crystal field split states. All three can contribute to the overall dielectric dispersion curve, thou magnons can only contribute if coupled to an electronic state through what is called an electromagnons [38]. As long as there is no interaction between the excitations then their contribution to the dielectric function can be expressed as a linear superposition of their individual electric susceptibilities:

$$\varepsilon(\omega) = 1 + \chi_{VE}(\omega) + \chi_{FC}(\omega) + \chi_{LV}(\omega) + \chi_{CF}(\omega) + \ldots, \tag{2.6}$$

where the 2nd term is due to bound valance electrons and can be assumed frequency independent in the infrared and is usually combined with the 1st term to form the high frequency dielectric constant (ε_∞) [29]. The 3rd term accounts for free carriers, however since only insulators will be considered, this term is not applicable to our case. The last two terms are the contributions from the lattice vibrations (phonons) and crystal field

transitions, respectively. Note the possibility is left for other contributions such as from the above mentioned electromagnons. Equation 2.6 can now be rewritten into a reduced form:

$$\varepsilon(\omega) = \varepsilon_{\infty} + \chi_{LV}(\omega) + \chi_{CF}(\omega) + \ldots \tag{2.7}$$

The dielectric property of a material is its response to an applied electric field at the crystal lattice level, whereby the field generates a displacement of charges or dipole reorientation. Modeling of the system can then be preformed using a damped harmonic oscillator model driven by the applied electric field (in our case the incident electromagnetic radiation). The dielectric function can be represented as a combination of the high frequency dielectric constant and the summation of the independent damped harmonic oscillators, see Equation 2.8. This is known as the "three parameter" or Lorentzian dielectric function model, where the S_j, γ_j and Ω_j are the strength, damping, and frequency of the jth oscillator [39,40,29].

$$\varepsilon(\omega) = \varepsilon_{\infty} + \sum_{j}^{N} \frac{S_j \Omega_j^2}{\Omega_j^2 - \omega^2 - i\gamma_j \omega} \tag{2.8}$$

Particularly important to the understanding of the ordering parameters involved in low temperature phase transitions is the behavior of oscillator modes (excitations) present in the FIR spectra. The onset of a ferroelectric (FE) phase is accompanied by a spontaneous polarization along a crystallographic direction by means of a distort of the crystal lattice or by the displacements of its ions. A phonon mode associated with these ions, according to "lattice dynamic theory", should experience a "softening" where by the square of its frequency tends towards zero. This what is known as a "soft mode" its

behavior can be express as a combination of Curie – Weiss law (Equation 2.9), which describe the temperature dependence of the static dielectric constant above a critical temperature T_c (for this reason T_c is also called the Curie temperature), and the Lyddane-Sachs-Teller (LST) relations (Equation 2.10), which states that the static dielectric constant tends towards infinity for a FE transition, while the transverse optical mode tends towards zero. This gives Cochran's law (Equation 2.11) and a correlation between the optical active phonons and the dielectric function.

$$\varepsilon_0 = \frac{4\pi C}{T - T_c} \tag{2.9}$$

$$\frac{\varepsilon_0}{\varepsilon_\infty} = \frac{\omega_{LO}^2}{\omega_{TO}^2} \tag{2.10}$$

$$\omega_{TO}{}^2 = \frac{\varepsilon_\infty \omega_{LO}{}^2}{4\pi C}\left(T - T_{critial}\right) \tag{2.11}$$

Since, MF also experience an ordering of their magnetic moments e.g., during their AFM phase transition, the incident electromagnetic wave can perturb the moments orientation can generate a magnon excitation. A magnon being the propagation of a spin wave is due to the strong exchange interaction between adjunct spins [41].

Lastly, there may be excitation modes related to transitions between crystal field (CF) split states from the rare-earth ions, as shown in Figure 2.4. The "crystal field" is an inhomogeneous field produced by neighboring ions in the lattice. In lanthanides, the rare-earth ions are stripped of their outermost 6s electrons, which leave the optically active 4*f* orbitals inside the filled 5*s* and 5*p* shells; this shields 4*f* orbitals from the crystal field. Consequently, this reduces its effect allowing for the crystal field to be treated as a

perturbation of the Hamiltonian. The CF is substantially smaller then the spin-lattice interaction which varies as Z^4, where Z is the number of electrons. Dipolar transitions can then occur between the low energy excited crystal field split states within the multiples. The importance of oscillator strength in crystal field split IR-active modes is analogous to the transition probability between split states to those of classical oscillating electrons [42].

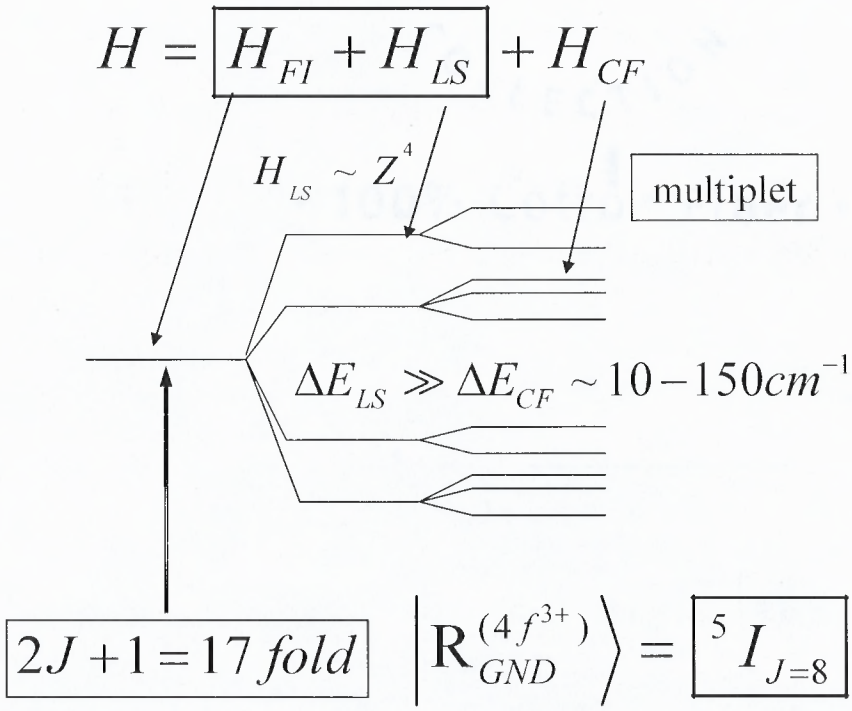

Figure 2.4 Diagram of the ground state splitting into multiplet levels for the case of a rare-earth (R) ion placed within a crystallize lattice. The Hamiltonian (H) consists of the free ion (H_{FI}) and spin-orbit (H_{LS}) terms along with a crystal-field (CF) perturbation (H_{CF}) term. Because of the large number of electrons (Z=58-70) the spin-orbit interaction is much stronger then the crystal-field; therefore, the CF term can be treated as a perturbation. ΔE_{CF} is the approximate energy between CF split multiple states.

CHAPTER 3

SYNCHROTRON FACILITIES

The following chapter will outline the beamline setups, which we utilized at three different synchrotron light sources. Each synchrotron facility was chosen for its combination of unique characteristics as related to the desired characterization measurements. The end-user segment of the beamline can be tailored to the users specifications, therefore the following descriptions are limited to that used in this work.

3.1 A2 High-Resolution XRD Beamline at CHESS

The A2 beamline at Cornell High Energy Synchrotron Source (CHESS) was configured to perform High resolution x-ray diffraction (HRXRD) as depicted in Figure 3.1. The incident synchrotron beam was initially conditioned by a double-bounce Si (111) monochromator in a (+n –n) configuration aligned to pass a wavelength λ = 1.17745 Å. The angular spread of the beam incident on the first Si (111) monochromator crystal is $\delta\theta$

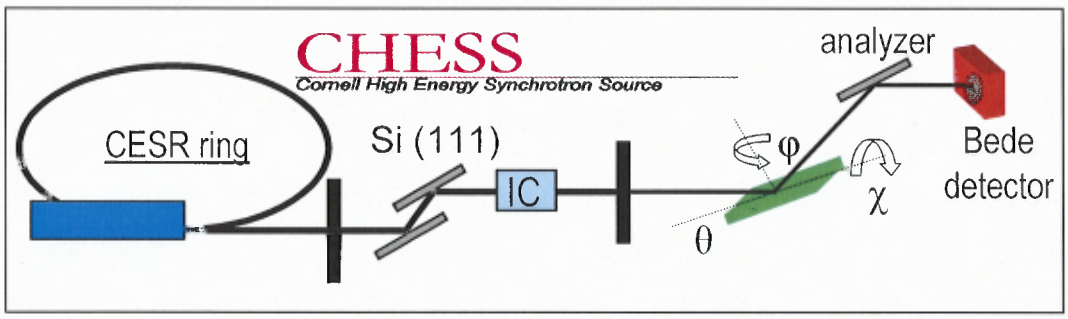

Figure 3.1 HRXRD setup at CHESS A2 beamline, where ω and 2θ denote rotation angles of the sample and detector arm, respectively. Ionization chambers for monitoring the beam intensity and slits for background fluorescence reduction and beam size.

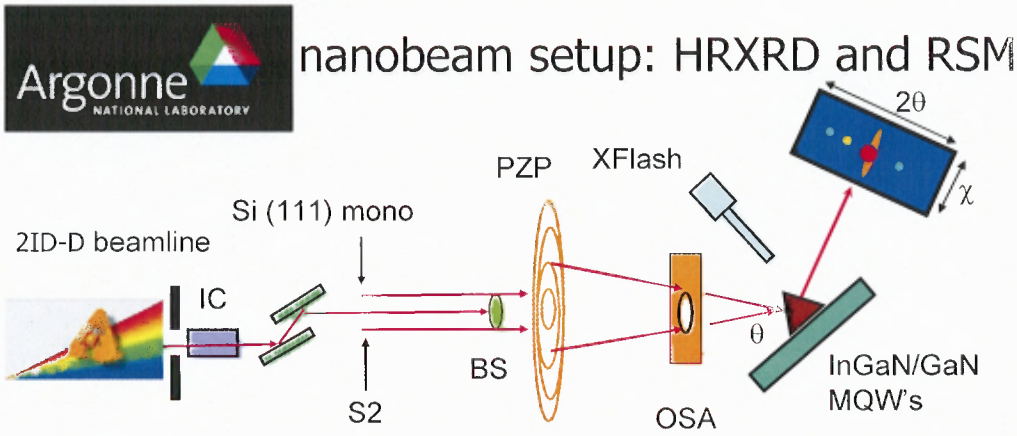

Figure 3.2 Nano-beam XRD setup at APS 2-ID-D beamline. Si(111) monochromator, gold beam stop (BS), phase zone plate (PZP), order sorting aperture OSA, XFlash fluorescence detector, CCD detector.

~ 5 arc sec, determined by the source size (0.3 mm) and the a 0.5 mm slit located 32.5 m upstream of the 49 pole wiggler. The samples were mounted in a four-circle Huber diffractometer, equipped a with high precision XY piezoelectric stage (Physik Instrumente) with the 50 nm accuracy. A pair of orthogonal slits positioned before the diffractometer determines the spot size on the sample. The scattered beam is conditioned by a single-bounce Si (111) analyzer crystal, and before being collected by a BEDE scientific scintillation detector with enhanced dynamic range. If desired, the beamline can be equipped with condensing and focusing capillaries to produce x-ray micro-beams, of the order of 8 μm.

3.2 2-ID-D nano-XRD Beamline at APS

The 2-ID-D micro-diffraction beamline at the Advanced Photon Source (APS) of Argonne National Laboratory (ANL) was equipped with a zone plate utilized to focus the x-ray beam to a semi-circular spot with a diameter of ~ 240 nm, see Figure 3.2. The

approximately 160 arc sec divergence of the beam has limited the angular resolution of our measurements [43]. Samples were mounted on an XYZ stage, which enabled real space mapping measurements. The position of the x-ray beam on the sample surface was controlled with 50 nm precision by monitoring of the Ga-*K* fluorescence from the ridges. Diffracted intensity was collected by a large-area CCD detector positioned on the 2θ arm of a Newport diffractometer. The resolution along both the 2θ and χ directions corresponded to ~16 arcsec, limited by the inter-pixel distance.

3.3 U12IR Far-Infrared Beamline at BNL

At NSLS the U12IR beamline radiation is taken from the storage ring through wedged diamond windows. The source is coupled to the beamline equipment with a 1:1 mirror box. Below 1000 cm^{-1}, which is the spectral range of the primary interest, the source is diffraction limited. Beamsize in the horizontal plane is limited by the slits. The beam divergence ϕ in the vertical direction is $\phi \approx 1.6 \cdot \left(\frac{\lambda}{\rho}\right)^{\frac{1}{3}}$, where ρ is the bending radius of the machine. For example, for λ = 0.19 cm (5 cm^{-1}), $\phi = 0.16$ rad. Spot size on the sample, *d*, for diffraction limited situation: $d \approx \left(\frac{1.2\lambda}{\sin\phi}\right)$, which results in $d \approx 8\lambda$ for f4 and $d \approx 30\lambda$ for f10 focusing optics. The beamline is equipped with a Fourier transform far infrared spectrometer: Bruker 125 (6 meter) with resolution of 0.002 cm^{-1} and acceptance beamsize of 75 mm. The detector consists of a liquid helium-cooled bolometer, used for IR signal measurements between 4 cm^{-1} and 700 cm^{-1}. Figure 3.3 depicts a schematic of beamline setup.

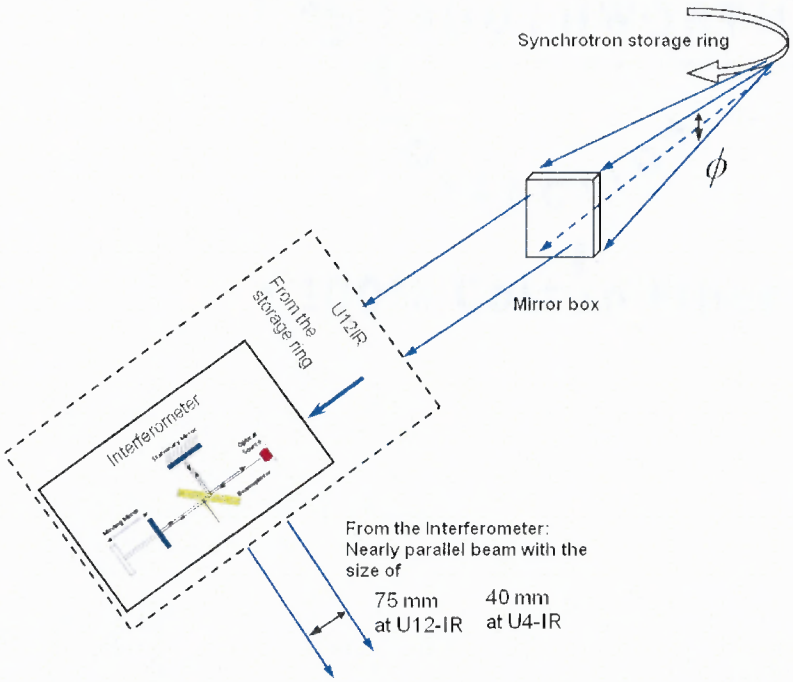

Figure 3.3 Schematics of IR beamlines at NSLS. U12IR beamline at NSLS/BNL, equipped with a high-resolution Bruker 125 interferometer and a low-temperature Oxford optical cryostat.

CHAPTER 4

InGaN/GaN MULTIPLE QUANTUM WELLS

The following Chapter details results of synchrotron radiation-based x-ray diffraction of InGaN/GaN MQW device structures grown on trapezoidal ridge structures. The driving force behind this work is the overall lack of knowledge on the period, strain, and composition of MQW layers growth on semi-polar sidewall facets of GaN trapezoidal ridges. Results were interpreted within the frame work of growth dynamics present during selective-area MOVPE growth. Special attention was paid to the role of surface migration versus gas phase diffusion effects in subsequent formation of the MQW layers on the GaN ridge structures.

Portions of this work have been published in:

- S. M. O'Malley, P. L. Bonanno, T. Wunderer, P. Brückner, B. Neubert, F. Scholz, A. Kazimirov, and A. A. Sirenko, "X-ray diffraction studies of selective area grown InGaN/GaN multiple quantum wells on multi-facet GaN ridges", phys. stat. sol. (c) **5**, 1655-1658 (2008).
- P. L. Bonanno, S. M. O'Malley, A. A. Sirenko, A. Kazimirov, Z.-H. Cai, T. Wunderer, P. Brückner, and F. Scholz, "Intra-facet migration effects in InGaN/GaN MQW structures grown on triangular GaN ridges studied by submicron beam X-ray diffraction", Appl. Phys. Lett., **92**, 123106 (2008).

4.1 Overview

The optical efficiency of InGaN quantum well (QW) devices has been hindered by the presence of large piezoelectric fields within the active region [2]. One way to reduce this problem is to grow QWs on semi-polar planes instead of the commonly used (0001) *c*-plane [6]. Access to these semi-polar planes, for subsequent growth, however is limited to

the following sources: (i) exotic substrate materials like γ-LiAlO(100), (ii) Si(111) substrates, (iii) bulk single crystal m-plane and a-plane GaN and (iv) trapezoidal/triangle shaped GaN ridge structures formed by selective-area-growth technique. Options (i-iii) have little practical use in commercial applications for either poor morphology and/or cost concerns. Option (iv) utilizes a process known as selective-area-growth (SAG), whereby GaN is grown between dielectric masks patterned on the substrate surface forming GaN ridges with semi polar sidewall facets. The sidewall facets provide an ideal plane for the subsequent growth of QW structures with reduced piezoelectric fields [6]. Currently, most research groups have relied primarily on photoluminance and imaging techniques e.g., scanning electron microscopy (SEM), to study the sidewall growth [44]. However, such techniques only provide limited information on the structural parameters of the active region. X-ray diffraction would be an ideal characterization tool in determining the structural parameters, e.g., layer thickness, strain, and composition. However, the x-ray source tubes used in commercially available diffractometer are too weak to adequately detect the weak signals originating form these narrow structures. In this case, the high intensity and large flux densities characteristic of synchrotron radiation provides an excellent source for performing XRD on these new device structures. In this chapter synchrotron based high resolution x-ray diffraction (HRXRD) was used to examine the influence of mask width and orientation on the period and strain of InGaN/GaN MQW growth on both top and sidewall facet planes. Results were interpreted within the framework of vapor phase diffusion and surface migration effects.

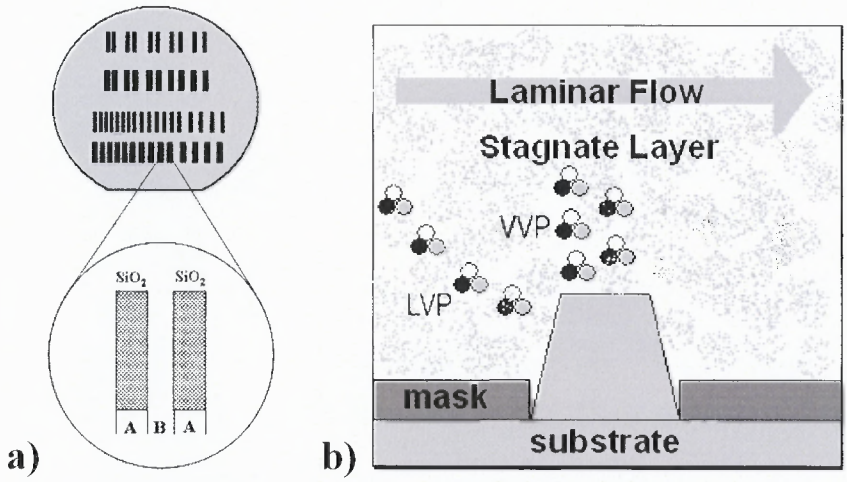

Figure 4.1 Schematic representation of the three transport mechanism involved in SAG: lateral vapor phase (LVP) diffusion, vertical vapor phase (VVP) diffusion and surface migration (SM). Gray areas above the black masks are to signify regions of greater precursor concentration.

4.2 Selective Area Growth (SAG)

The SAG technique has been implicated in many different growth regimes, however it's primarily utilized in MOVPE growth. In traditional MOVPE growth, precursors diffuse vertically through a "stagnate" layer of a few hundred microns thick before reacting with the substrate [45]. MOVPE-SAG can be realized due to the fact that growth does not take place on the surface of the oxide masks; this creates an accumulation of precursors in the gas phase, immediately above the masked regions. The accumulation can thereby supply source material to the unmasked regions where it can contribute towards growth. Transport in SAG occurs via three mechanisms: vertical vapor phase (VVP) diffusion, lateral vapor phase (LVP) diffusion, and surface migration (SM). Figure 4.1 is a schematic representation of these mechanisms, each with different characteristic lengths that result in the thickness enhancement and compositional changes in the SAG regime. Lateral vapor phase (LVP) diffusion arises because of the horizontal concentration

gradient of precursors created by the masked and unmasked regions. The large V/III ratios needed for good layer morphology of group-III nitrides, implies that growth is limited by the supply of group-III species.

The gas-phase diffusion model allows accurate calculations of the VVP and LVP effects with characteristic diffusion lengths D_v/k in the range of 20–200 μm, while the surface migration effect is important for the analysis of the ridge shape and composition on the scale of a few microns. Model the growth enhancement attains a simplified form in the case of a periodic array geometry for the oxide mask formation. Indeed, the gas-phase diffusion model, which otherwise requires the knowledge of the diffusion lengths D_v/k for the group-III precursors (In, Ga), has a simple analytical solution for periodic arrays. In this case, the growth enhancement P/P_0 can be expressed according to the law of conservation of source material in periodic arrays, where the enhancement is limited by the mask load and for the SAG process with $D_v/\mathrm{k(In,Ga)} \gg A+B$, where A is the mask width and B is the window width. In this case the MWQ period thickness (P) can be written as:

$$P = P_o \frac{(A+B)}{B}, \tag{4.1}$$

where P_0 corresponds to the unmasked growth in the field. Figure 4.2 is a plot of equation 4.1 for various window and mask widths. Note the linear dependence on mask width and the stronger enhancement with diminished window width as expected for the increase in source material concentration with smaller growth areas.

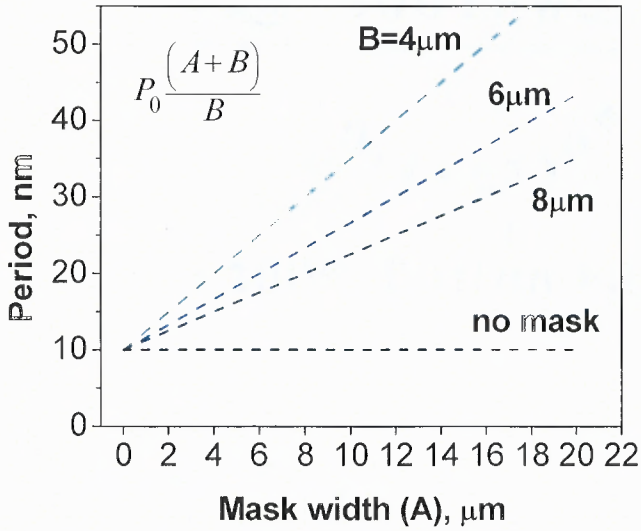

Figure 4.2 Plot depicts the growth enhancement of the MQW period as a function of the mask width A.

4.3 Sample Growth and Describtion

Samples were grown by the Ferdinand Scholz's group at the University of Ulm, Germany, using low-pressure MOVPE in a single-wafer Aixtron system with a horizontal reactor design. Trimethyl gallium (TMGa), trimethyl indium (TMIn) and ammonia (NH3) as the precursors with H_2 carrier gas. A GaN buffer layer was grown epitaxially on *c*-plane sapphire (Al_2O_3) substrates, which were exposed to a nitrogen rich atmosphere sequentially producing an AlN nucleation layer. The dielectric mask pattern was created by growth of an oxide layer of SiO_2 (200 nm thick) on the GaN buffer layer by PECVD and patterned by optical lithography and reactive ion etching. Then, n-doped GaN ridges were grown inside the unmasked regions with growth conditions optimized for triangular/trapezoidal shaped ridges. The MQW structure was then grown on the GaN ridge structures, consisting of five InGaN quantum wells separated by GaN barriers. Reactor temperature was reduced from 1020°C to 800°C, for better Indium incorporation

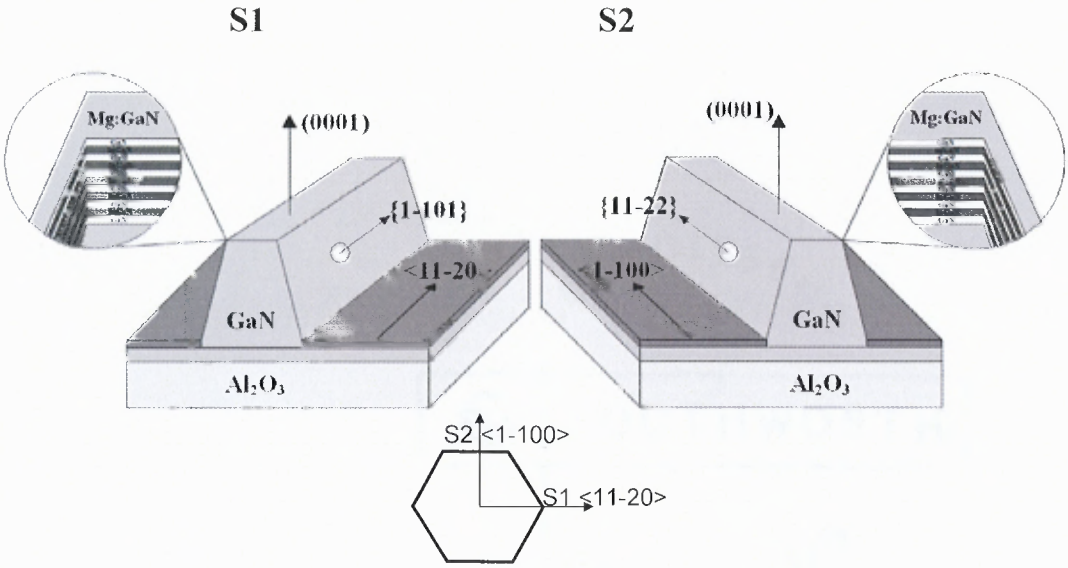

Figure 4.3 Schematic representation of the InGaN/GaN MQW structure for sample S1 and S2, with oxide mask (dark gray) direction and sidewall facets depicted. Circular insert shows growth of the InGaN/GaN MQW followed by a Mg: GaN capping layer.

in the MQW active regions. Lastly, the device structure was finished with a p-doped GaN:Mg capping layer with a target thickness of ~0.2 μm, grown at 1020° C, and using CP_2Mg as the dopant. Two mask orientations were chosen: sample S1 had masks oriented parallel to the <11-20> crystallographic direction and sample S2 along the <1-100> direction. The ridge sidewall facets depend on mask direction, thus, S1 has {1-101} sidewall facets and S2 {11-22} sidewall facets. Mask design was selected to produce arrays of identical GaN ridges, where the mask width A varies from A= 2 to 20 μm in 2 μm steps, and the unmasked (window) width B is fixed at either B= 4, 6, or 8 μm.

4.4 Measurement Parameters

High-resolution x-ray diffraction (HRXRD) was performed at the A2 beamline of Cornell High Energy synchrotron Source (CHESS). The incident synchrotron beam was initially conditioned to an energy of E = 10.531keV. The samples were mounted in a four-circle

Huber diffractometer, with ridges oriented along the diffraction plane. The scattered beam was conditioned by a single bounce Si (111) analyzer crystal and collected by a BEDE scintillation detector. A pair of orthogonal slits positioned before the sample determined the beam size, 0.2 × 0.2 mm^2, incident on the sample surface. This allowed several identical ridges within a particular array group to be probed simultaneously. The sidewall facet grown were probed by rotating the sample about an angle chi (χ), thus bringing the sidewall MQW perpendicular to the diffraction plane, thereby enabling coplanar θ-2θ scans. Sample S1 with its {1-101} sidewall facets was rotated to $\chi = 61.9$ deg, while S2 {11-22} was rotated to $\chi = 58.4$ deg.

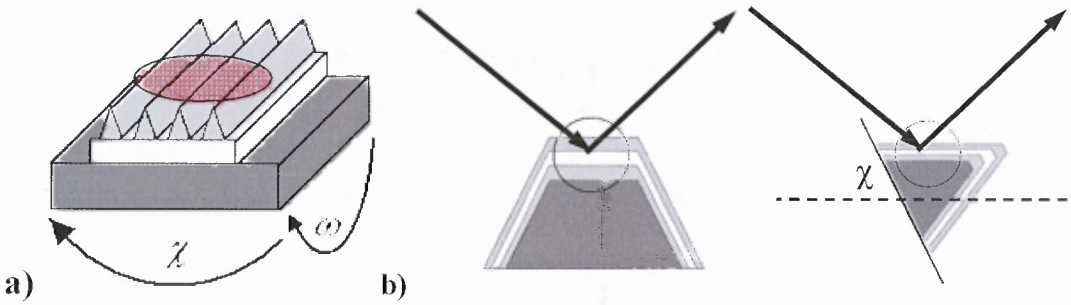

Figure 4.4 (a) Schematic illustrating the angular freedom of the sample once mounted into the diffractometer. Red circle symbolizes that several ridge structures were probed at once due to 0.2x0.2 mm^2 spot size. (b) Depictions the surfaces struck by x-ray beam facilitating coplanar reflections from the top and sidewall facets, respectively.

4.5 HRXRD Results from the Conventional (0001) Plane

A series of longitudinal ω-2θ diffraction curves and RSM systematically carried out on both samples for varies mask and window widths. The (00.2) and (00.6) symmetric reflections were chosen to probe top facet growth; the former, for its greater scattering

signal and the latter because of its increased sensitivity to strain [46]. In our first experiments several ridges were probed at once, including the top part and the sidewalls of the ridges, but due to the application of the high resolution analyzer all symmetric reflections were only sensitive to the structure periodicity along the surface normal. Therefore, the (00.2) and (00.6) reflections are only measuring MQW growth on the tops of the GaN ridges. The Bragg condition for GaN was satisfied at an angle $\theta_{00.2}$ (GaN) = 13.142° at the incident x-ray wavelength, which corresponds to q_z = 3.863 nm^{-1} in reciprocal lattice units. Figure 4.5 depicts the θ-2θ diffraction scans from the 6 μm wide mask opening of samples S1 and S2. MQW peaks associated with the presence of structural grown on the top (00.1) plane can clearly be seen for both mask orientations.

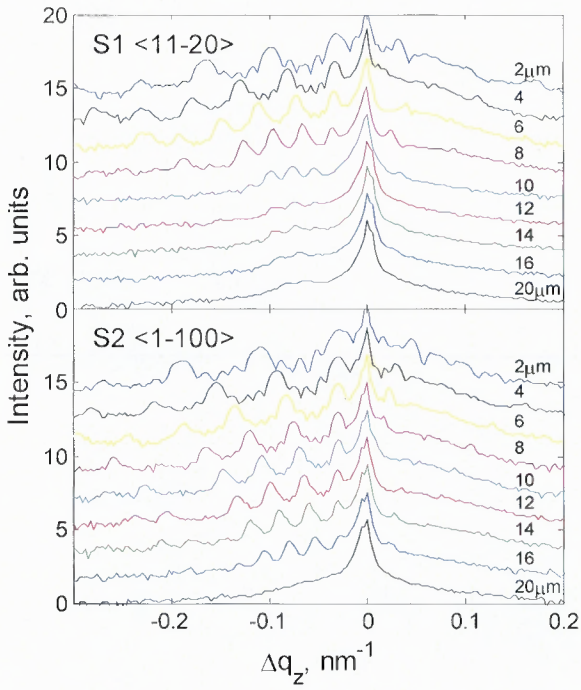

Figure 4.5 θ-2θ scans for symmetric (00.2) reflections from samples S1 (top) and S2 (bottom) for 6 μm wide openings with mask width *A* varied from 2 μm (upper curve) to 20 μm (lowest curve). Intensity shown in log scale and horizontal axis is presented in relative reciprocal lattice units (q_Z [00.2] = 3.863 nm^{-1}). Diffraction curves are vertically offset for clarity.

Interstitial *N-2* Kiessig fringes (maxima) are visible for narrow mask widths, attesting to the high angular resolution of the diffractometer setup and effective suppression of the diffuse background. The signal of the MQW peaks diminishes noticeably, as it converges into envelope function profile, with increased mask width in both samples. Sample S2 manages to retain its peak visibility up to larger widths (A = 16 μm), with its mask orientated along the <1-100> direction. The diffraction curves have been plotted in reciprocal lattice units to facilitate comparison between curves measured with different wavelengths (e.g., the case where preliminary measurements are preformed in our in-house Bruker D8 diffractometer equipped with x-ray (λ=1.540Å) prior to going to the synchrotron where typically a different wavelength is chosen) in that the curves now wavelength independent. Plotting the diffraction signal versus relative reciprocal lattice units is also beneficial by simplifying the formulas used in determining the MQW global strain and period parameters as follows, by removing the trigonometric functions and dependence on wavelength, see Equations 4.2 and 4.3.

$$S_{\perp} = \Delta\theta \cot\theta_B = \frac{\Delta q}{q_L} \tag{4.2}$$

$$P = \frac{\left(L_i - L_j\right)\lambda}{2\left(\sin\theta_i - \sin\theta_j\right)} = \frac{\left(L_i - L_j\right)}{\Delta q_{ij}} \tag{4.3}$$

Values of strain S are presented in the units of the d-spacing mismatch. MQW periods were determined by measuring separation between adjacent SL peaks according to Equation 4.3. Figure 4.6a compares the periods (P) for samples S1 and S2 at various mask widths for the top (0001) planar growth from 6 μm wide ridges. Both samples show an initial linear dependence of period with mask width (A). As width is increased, sample

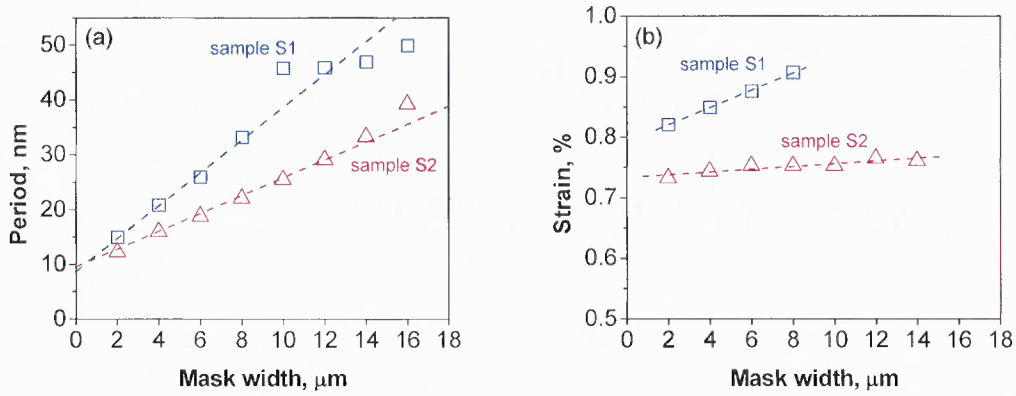

Figure 4.6 (a) MQW period versus Mask width *A*, for S1 (blue) and S2 (red), with 6 μm wide ridges. (b) Global MQW strain for S1 and S2, determined using Equation 4.2. The dashed lines depicts the linear trends. Only results from the (00.2) reflection are shown.

S1 experiences the onset of saturation for width values greater then 8 μm. Sample S2, displays a linear dependence for almost the entire range, deviating only slightly at the largest mask widths. The MQW strain as determined by Equation 4.2, is shown in Figure 4.6(b). A significant increase in strain for S1 can be seen in contrast independent behavior of sample S2. The quasi-linearly strain dependence of S1, from S= 0.82% to 0.91%, with mask width. This is in contrast to S2 that is comparatively mask independent, only ranging from S= 0.73% to 0.76%. Note that the strain determination in S1 was not possible beyond 8 μm due to the disappearance of the 0th order MQW peak and subsequent uncertainly in peak position. Reciprocal space maps in Figure 4.7(a, b) demonstrate that the strain in the measured ridges is indeed elastic.

Comparison of these results for the 6 μm widow structures with that from other sized window openings reveals that the MQW related diffractions peaks are less prominent at the smaller 4 μm openings. This trend can be seen in Figure 4.8 where the 4 μm sized ridges in sample S1 contain only the strong GaN substrate peak and show no

signs of MQW related peaks. Results from the larger 8 μm opening demonstrate that the MQW signal persists longer with increasing mask width then in the case of the smaller openings. Unfortunately during cleaving of the sample wafer in various sections for

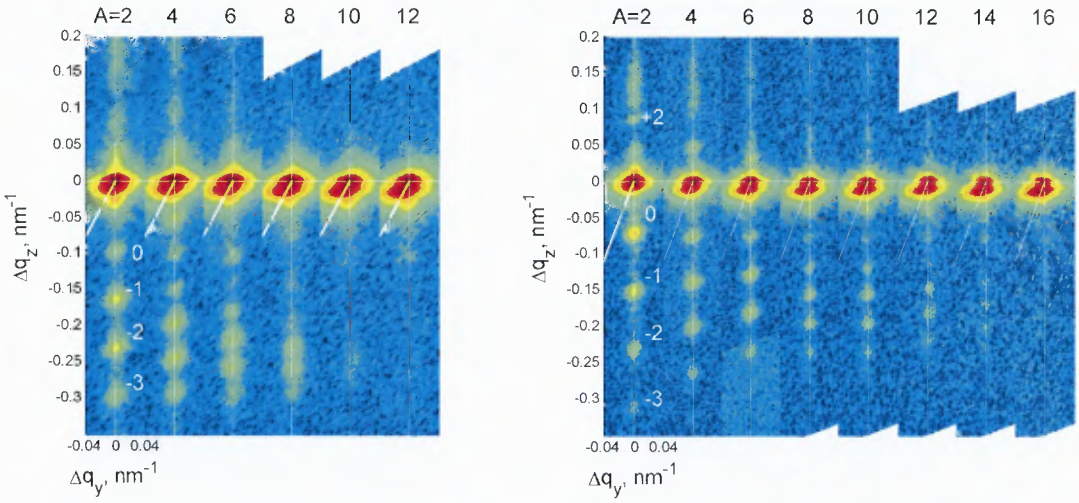

Figure 4.7 Combined reciprocal space maps for the asymmetric (11.6) and (10.5) reflections from top ridge grown MQW for samples S1 and S2, respectively. The MQW satellite peaks for both samples are aligned parallel to the growth direction, indicative of a fully (elastically) strained MQW structures.

analysis most of the 8 μm section of sample S2 was damaged; hence, explaining the lack for diffraction curves in the last plot of Figure 4.8. Comparing the growth enhancement behavior in Figure 4.8 one can notice that in the case of sample S1 saturation of growth enhancement has been suppressed at the large window opening while the sample quickly experiences saturation for the smaller 4 μm opening.

Scans from S1 with 4 μm ridges in Figure 4.8 showed only the GaN substrate peak; no visible SL peaks were present. Sample S2, however, did have SL peaks, visible up to the maximum 20 μm wide oxide mask width. Sidewall growth was examined using the (20.2) reflection from {1-101} sidewall facets of S1 and the (11.2) reflection from

{11-22} facets of S2. In both samples, sidewall SL peaks are present for the narrower 4 μm wide ridges.

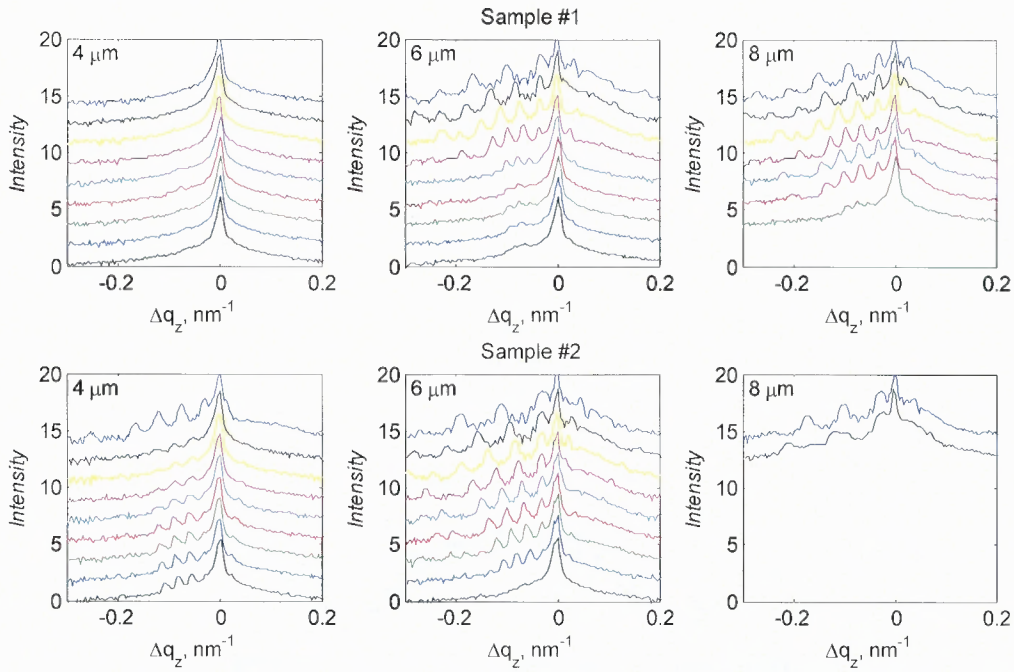

Figure 4.8 θ-2θ scans for the symmetric (00.2) reflection form S1 (top set) and S2 (bottom set); for ridge widths 4, 6, and 8 μm (from left to right) with mask width varied form 2 μm (upper curve) to 20 μm (lowest curve) in 2 μm steps. The horizontal axis is presented in relative reciprocal lattice units (q_z [GaN] = 3.863 nm^{-1}). Diffraction curves are vertically offset for clarity.

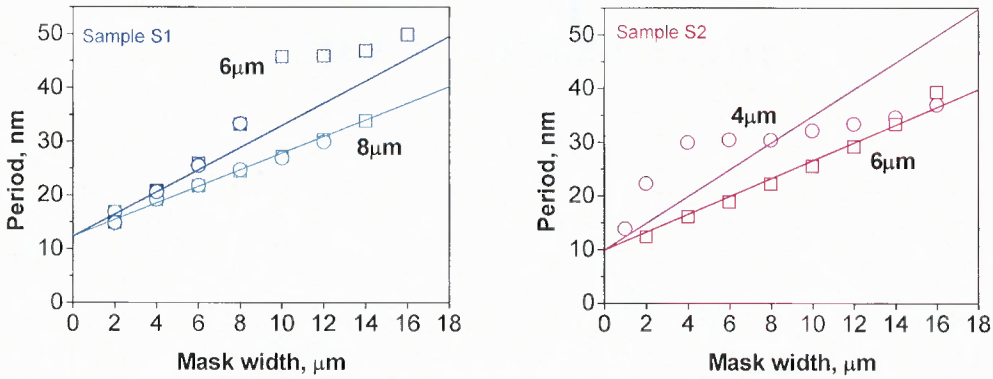

Figure 4.9 Comparison of MQW period versus mask width (*A*) for different window widths (*B*). Where available both the (00.2) and (00.6) results are shown. The solid lines are the expected period thicknesses as determined by the conservation of source material model, see Equation 4.1.

4.6 HRXRD Results from Faceted Sidewall Planes

Variation of the MQW period for top and sidewall growth is shown in Figure 4.9a for both the 4 and 6 μm wide ridges from sample S2. Comparison between the top and sidewall growth reveals a lateral / vertical growth rate ratio of ~0.3. The growth enhancement is stronger for the narrower 4 μm opening with an earlier onset of saturation. The global MQW strain values for the 4 μm ridges from S2 were $S \sim 0.78\%$ and 0.59%, for top and sidewalls growth, respectively, which corresponds to an approximate 24% reduction in strain for the sidewall grown MQW structure. Figure 4.11b compares sidewall periods for samples S1 and S2 with 4 μm wide openings.

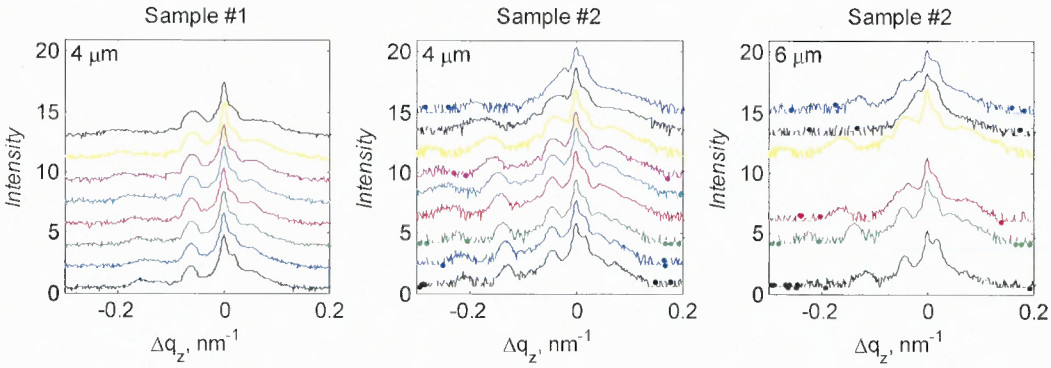

Figure 4.10 Coplanar θ-2θ scans form the sidewall facets of samples S1 and S2, using the (20.2) and (11.2) reflections respectively. The sidewall was brought in the diffract plane by rotating sample S1 by χ=58.4° and sample S2 by χ=61.9°. Ridge widths are 4 μm for S1 and 4 and 6 μm for S2 (from left to right) with mask width varied form 2 μm (upper curve) to 20 μm (lowest curve) in 2 μm steps. The horizontal axis is presented in relative reciprocal lattice units, q_z (20.2) = 8.201 nm^{-1} and q_z (11.2) = 7.370 nm^{-1}.

4.7 Fitting Diffraction Curves

When comparing MQW periods between the two mask orientations (Figure 4.6a), the larger slopes for S1 indicts stronger growth rate enhancement with its <11-20> orientated mask than S2 with <1-100> mask orientation. The common interpolated intersect at $A = 0$

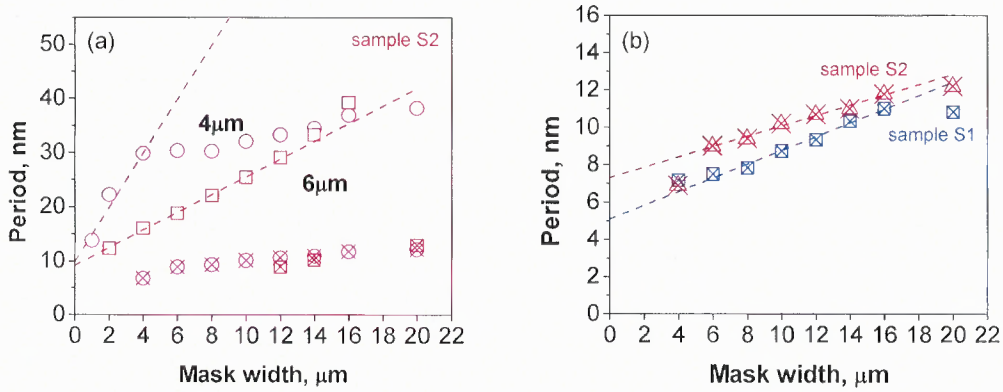

Figure 4.11 (a) MQW period for sample S2 from the top (open) and sidewall (open + cross) growth (b) Period comparison between sidewall grown MQW from S1 and S2 with 4 μm opening. Dashed lines depicts linear fit.

reinforces the fact that both samples were grown under the same reactor conditions. Growth enhancement for samples with identical mask pattern and reactor conditions ought to have similar structural parameters under the law of source material conservation based on the gas phase diffusion of precursors towards the growth surface. Therefore, results in Figure 4.6, which clearly highlight the difference in strain and growth enhancement, indicate that other considerations must be taken into account, such as the exact ridge dimensions and inter-facet migration of group-III species. Relating ridge profile evolution obtained by SEM (Figure 4.12) to the MQW period dependence observed in Figure 4.6a suggests that S1 $B = 6$ μm experiences a "shape transition" with increasing mask width, from a trapezoidal to triangular shape at $A \sim 8$ μm. The diminishing visibility of MQW satellite peaks with increased mask width and a constant MQW period for $A \geq 10$ μm corresponds to termination of the sidewall growth at the apex of triangularly shaped ridges. The 6 μm wide ridges of S2 do not experience a full evolution to a triangular profile and therefore, do not experience saturation in growth

enhancement. The conservation of source material equation used to model the growth enhancement assumes an ideal rectangular ridge profile. Therefore, the top ridge width (b) should be identical to the opening width (B), Figure 4.12. However, SEM images revealed that b is in fact less then B. The smaller ridge tops should then experience significantly larger growth enhancement than that predicted using B in the model. Further complicating matters is the overgrowth experienced in the SAG of GaN. This overgrowth, commonly referred as "wings," reduces the masked width A [4]. In spite of these discrepancies, there is surprisingly good agreement between the growth enhancement model and actual experimental data for the S2 6 μm width ridges. The sidewall facet growth may have contributed to this agreement by reducing the overall concentration of group-III precursors over the ridge tops.

Fitting the θ-2θ scans for top ridge growth using commercially available RADS Mercury Bede software produced an indium concentration for the InGaN quantum wells was determined to be 12.5% for S1 and 11.5% for S2; these values were independent of mask width. The fitting, using the dynamic theory of x-ray diffraction, allowed for decoupling of the well and barrier thicknesses [5]. This revealed that InGaN wells in S1 grow faster than the GaN barriers. The global MQW strain in S1, which increases with mask width, is due to the larger well growth rate. Sample S2 growth rates for well and barrier were fairly similar, explaining the samples relatively constant strain dependence. The difference in growth rates, and the strain dependence found between the samples, may be due to inter-facet migration effects, where indium can migrate further on the {1-101} sidewall facet of S1 and contribute to growth on the top (0001) ridge plane.

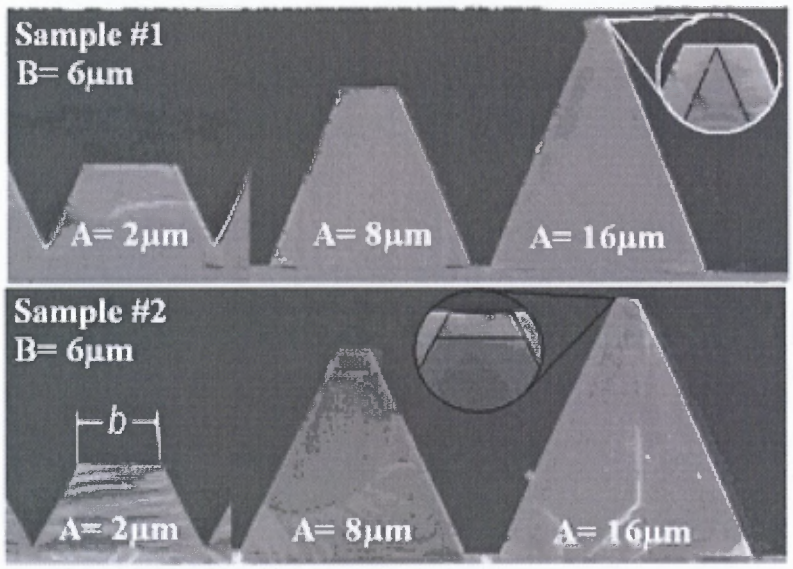

Figure 4.12 Cross-sectional TEM images taken from a single ridge structure within the array for both samples S1 and S2. The insert provides a magnified view of growth at the apex. The lines were used to highlight the interfaces. The distance *b* is the actual ridge base width. Note: the images were stitched together so the relative distance between ridges is representative of their actual spacing.

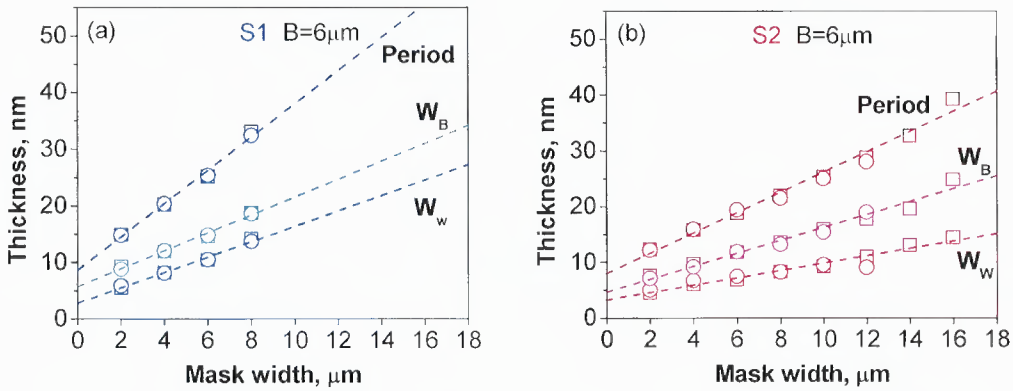

Figure 4.13 (a) Well (W_W), barrier (W_B) and period widths from the top facets growth for samples (a) S1 and (b) S2. The layer widths were determined by fitting the diffraction curves for both the (00.2) (open square) and (00.6) (open circle) reflections, using RADS Mercury software based on the Takagi-Taupin formalism.

4.8 Nano-Beam Reciprocal Space Mapping

In the previous paragraph we described the "average" properties of the MQW growth on the ridge sidewalls. In this section the sidewall growth was further investigated at the local scale by performing submicron-beam RSM across the ridge structure. The measurements were carried out at the 2-ID-D beamline at APS, as described in Section 3.2, where the use of zone-plate optics allowed for a 240 nm beam size, i.e., small enough spatially to attain several RSM along a single sidewall facet. This study allowed for local examination of variation in the period and strain along the ridge and intra-facet surface migration.

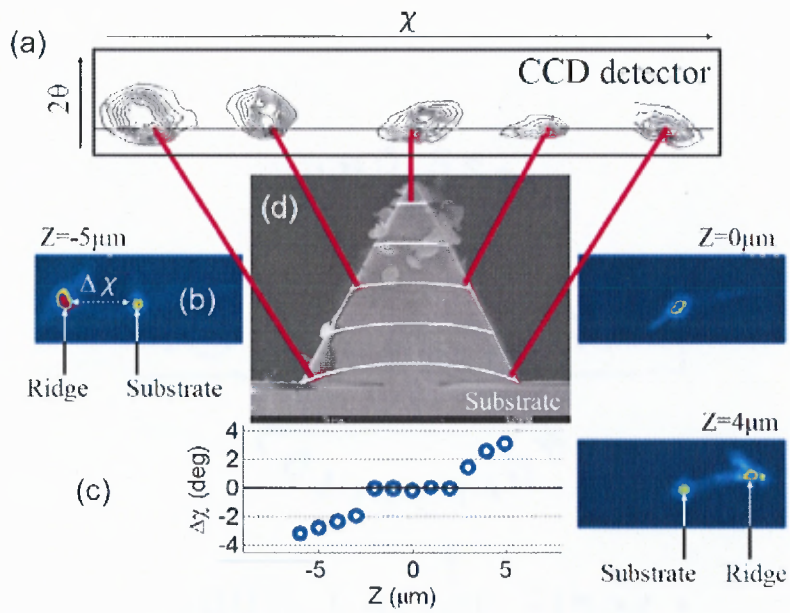

Figure 4.14 (a) A qualitative illustration of the tilt of the (00.1) planes observed as an azimuthal shift $\Delta\chi$ of the Bragg (00.2) reflection on the CCD detector. (b) An example CCD image shows the definition of $\Delta\chi$ as the difference in χ between (00.2) GaN reflection from the ridge and that from the substrate. (c) Azimuthal shift $\Delta\chi$ as a function of the position Z from the apex of the ridge. (d) SEM image of a single GaN ridge with tilt of horizontal (00.1) plane shown schematically with white curves.

In order to measure coplanar reflections along the entire sidewall, isolation of a single ridge would be needed, hence samples S1 and S2 were not suitable because of the relatively close proximity between ridges within an array. Therefore, a new sample S3 was growth with an array of identical ridge structures grown with a 3 μm window (B) and 10 μm wide masks (A). Sample S3 was prepared in the same manner as S1, with the mask orientated along the <11-20> direction; however, only 3 InGaN quantum wells where grown [47].

There is typically a significant amount of overgrowth of the GaN ridge on the oxide mask, as see in Figure 4.14. The overgrowth regions of the ridge known as "wings", is known to contain a significant tilting of its (0001) crystallographic planes [48]. No previous work (to the Author's knowledge) has studied this tilt locally along the ridge. Investigation into tilt present within the GaN ridge structures was made possible at the 2-ID-D beamline because of the large area charge coupled device (CCD) mounted on the 2θ arm of the diffractometer. With the ridges oriented along the diffraction plane, the presence of wing tilt, for a symmetric reflection, would correspond to a shift in the χ (chi) angle, represented as a lateral shift of the substrate peak within a single CCD image. This method saves a lot of time by not having to perform a RSM using a single channel detector for each new position along the ridge to gain local information on the wing tilt. Figure 4.14 represents tilt results measured across a ridge using the symmetric (00.2) reflection. The parameter Z is the relative displacement from the center of the triangular shaped ridge. Figure 4.14a depicts qualitatively the aforementioned lateral shift of the GaN Bragg peak within the CCD image. Figure 4.14b is a single CCD image containing both the untilted substrate peak and χ shifted signal from the ridge sidewall, where, $\Delta\chi$

represents an azimuthal shift form the Z=0 position which is equal to the degree of tilt of the (0001) planes. Figure 4.14c plots the tilt versus position of the x-ray beam across the ridge. The tilt increases as the beam moves away from the center of the ridge, where noticeable deviation from the central substrate signal occurs ~ 3 μm from the ridge center, and increasing quasi-linearly at a rate of ~ 0.6 deg/μm away from the apex, eventually reaching more than 3° by the edges of the ridge wings. The ultimate crystallographic tilt present within the ridge structure has been schematically depicted in Figure 4.14d by superimposing white line onto a SEM of the ridge profile.

The sidewall MQW growth was measured by rotating the sample about χ by 61.9° therefore fascinating coplanar RSM for the symmetric (1-1.1) reflection. The reciprocal

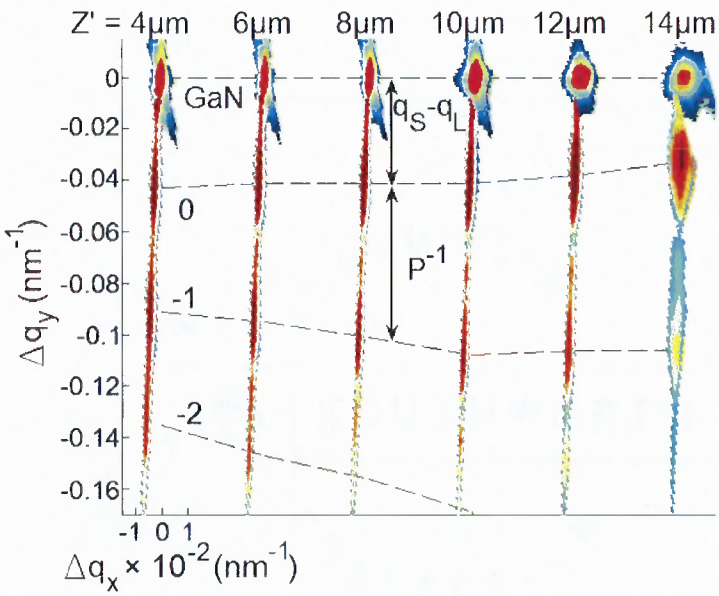

Figure 4.15 Reciprocal space maps for the (1-1.1) reflection measured along the ridge sidewall. The distance *Z'* from the apex of the ridge is shown in microns on the top of the plot. The MQW satellite peaks are marked according to their order. The FWHM of the satellites in q_x direction is comparable to the beam divergence (~160 arcsec) of our experimental setup.

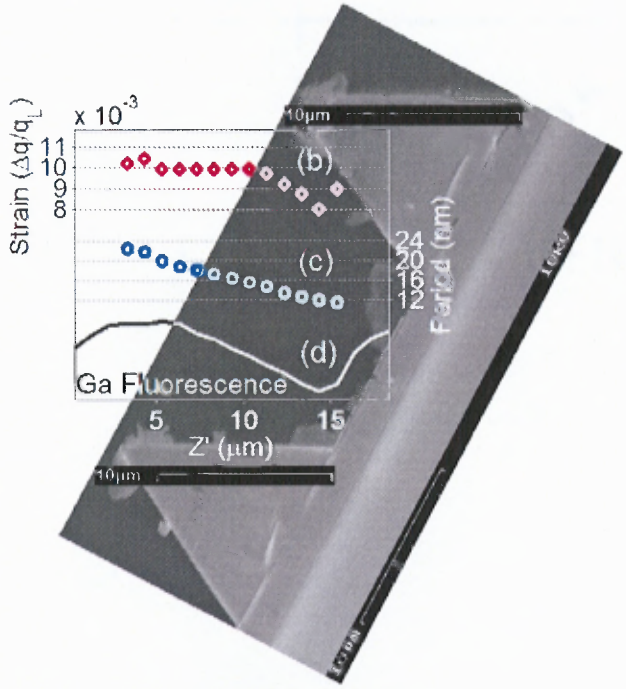

Figure 4.16 (a) SEM image of the ridge structure situated to correlate with the superimposed plot. (b) The MQW global strain (red diamonds) and (c) the period (blue circles) as a function of distance Z′ from the ridge apex. (d) the Ga fluorescence profile (solid line) measured across the ridge.

space maps were measured by collecting CCD images at intervals of θ about the Bragg condition θ_B=14.03°. Figure 4.15, depicts a series of RSM measured at several locations along the ridge sidewall. The dashed lines trace the movement of the MQW peaks in reciprocal space as a function of distance from the apex. This highlights the steady increase in peak separation which in real space relates to reduction in period moving towards the ridge base.

Figure 4.16 summarized the MQW period and strain results along the ridge. A sudden decrease in the global strain occurs at ~10 μm. One would not expect the composition to change abruptly; therefore, the relaxation is most likely due to the aforementioned tilting within the underline GaN crystallographic planes. In Figure 4.16c, the period maxim (22.5 nm) occurs at the ridge apex then begins to decreasing quasi-

linearly down the sidewall where it reaches a minimal value of 11.6 nm at the base. This strong variation in MQW period along the sidewall facet can be explained by a combination vapor phase diffuse and intra-facet migration effects. Both In and Ga precursors have a relatively short diffusion length (D_0/k~11 μm for Ga) [49]; because the ridge height ~10 μm, there most likely exists a supply gradient of source material along sidewall. Since the ridge apex is closest to the stagnant layer, it would experience the greater supply of precursors and hence a larger growth rate then the base. In the case of the GaN ridge growth, this asymmetry in growth would be suppressed by intra-facet migration. The higher growth temperature (1000°C) of the ridge growth would promote greater mobility of the group-III species along the sidewall length. The MQW layers however, were grown at 800°C, and therefore, the resulting diffusion and migration lengths would be reduced allowing for the variation in period observed along the ridge sidewalls.

4.9 Conclusion

The gas-phase diffusion model can qualitatively predict the top facet grown MQW period dependence for the larger window opening, however fails at the narrowest ridges. The difference between samples with orthogonally oriented masks, is another indication that other considerations must be taken into account, such as the exact ridge dimensions and inter-facet migration of group-III species. It was proposed that the difference in growth rates and strain dependence between samples, is due to inter-facet migration effects, where the group-III species can migrate further on the {1-101} sidewall facet and contribute to growth on the top facet plane. For the case of sidewall MQW growth, the

micro-beam XRD measures revealed an underlining GaN ridge containing a large tilt distortion of its lattice, which causes subsequent relaxation of the MQW strain near the ridge base. The strong variation in period along the ridge sidewall was attributed to both the relatively short diffusion length of the group-III precursors and inadequate intra-facet migration effects. The development of the synchrotron-based XRD characterization technique will be useful for the future GaN-based integrated photonic structures.

CHAPTER 5

MULTIFERROIC SINGLE-CRSYTAL $HoMn_2O_5$ RARE-EARTH MANGANITE

The following Chapter details a systematic study of the linearly polarization far-IR transmission spectra in the multiferroic manganite $HoMn_2O_5$. The spectra were measured at low temperatures in the vicinity of ferroelectric and antiferromagnetic phase transitions using synchrotron radiation-based Fourier transform infrared (FT-IR) spectroscopy. The observed IR-excitations have been attributed to electric-dipole transitions between ligand-field (LF) split states of Ho^{3+} ions. Also, the existence of possible composite excitation between magnon and excited LF states is proposed.

Portions of this work have been published in:

- A. A Sirenko, S. M. O'Malley, and K. H. Ahn, S. Park, G. L. Carr, and S-W. Cheong, "Infrared-active excitations related to Ho^{3+} ligand-field splitting at the commensurate-incommensurate magnetic phase transition in $HoMn_2O_5$", Phys. Rev. B, **78**, 174405 (2008).

5.1 Overview

Interplay between the long-range magnetic and ferroelectric ordering has recently motivated extensive studies of rare-earth multiferroic manganites RMn_2O_5 (R = Tb, Dy, and Ho) [50,51,52]. These materials are attractive for both fundamental studies and for possible device applications due to the intriguing phase diagram and magnetic field induced spontaneous electric polarization.

Recent optical studies of spin-lattice dynamics in multiferroics progressed in several directions: conventional Raman scattering spectroscopy of optical phonons [53,54], infrared (IR) spectroscopy of the phonons [55], as well as the low-frequency

excitations called "electromagnons" [56,57,58]. The report by Mihailova *et al.* [53] on the absence of optical phonon anomalies at the phase transitions in RMn_2O_5 (Ho, Tb) was followed by the observation of very small (< 1 cm^{-1}) anomalous shifts of the high frequency optical phonons around T_1 in R = Bi, Eu, and Dy compounds [54]. The spectra of the Raman-active optical phonons demonstrates only minute variations, IR-active excitations in $RMnO_3$ (R = Gd and Tb) [55] and $TbMn_2O_5$ [56,58] has shown intriguingly strong changes at low temperature phase transitions.

5.2 Sample Preparation and Description

The high-temperature flux growth technique was utilized to produce bulk crystals of $HoMn_2O_5$ at Rutgers University. The samples were prepared using a B_2O_3-PbO-PbF_2 flux in a Pt crucible where the mixture was held at 1280°C for 15h before being cooled down to 950°C at a rate of 1°C/h, further details can be found in Reference [50, 59]. The samples cross-sectional areas were approximately a few mm^2 in width and ~ 0.5 mm in thickness. The cryptographic orientations were determined using x-ray diffraction. The opposite sides were polished and wedged with a ~7° offset in order to suppress interference fringes.

$HoMn_2O_5$ experiences a number of low temperature phase transitions: upon cooling, Mn spins order in the *a-b* plane at $T_1 \approx 40 - 43$ K and incommensurate order of Mn spins switches to commensurate one at $T_2 \approx 37 - 39$ K and back to incommensurate order again at $T_3 \approx 15 - 25$ K. Finally, rare-earth spins order at lower temperatures below $T_4 \leq 10$ K. Anomalies in the dielectric constant and thermal expansion at T_1, T_2, T_3 and T_4, along with the appearance of spontaneous polarization along *b* axis at T_2 (the Curie

temperature), reveals changes within the ferroelectric order and provides evidence for strong spin-lattice coupling effects in RMn_2O_5 multiferroics [60].

5.3 Measurement Parameters

Transmission intensity was measured at the U12IR beamline at the National Synchrotron Light Source at Brookhaven National Laboratory equipped with an Oxford optical cryostat, Bruker 125HR spectrometer, LHe-pumped (~1.4 K) bolometer, and two grid polarizers for incident and transmitted radiation, respectively. The frequency resolution of 0.6 cm^{-1} was chosen to be about three times smaller than the typical width of absorption lines. Transmission intensity was measured with an incident beam perpendicular to the sample plane in various polarization configurations *z(x,y)*, where *z* is the direction of the light propagation, *x* and *y* denote electric polarization of incident and transmitted light, respectively. For each sample the raw data of transmitted intensity were normalized to transmission through an empty aperture with a size close to that of the sample.

5.4 Transmission Spectra of $HoMn_2O_5$

Figure 5.1 depicts the transmission spectra of $HoMn_2O_5$ measured in the *a(b,b)* , *b(a,a)* , and *a(c,c)* configurations at T = 5 K. The spectra are clearly dominated by several absorption lines at 10.5, 13, 18, 37, 42, 52, and 97 cm^{-1}. There also exists a couple of additional higher-frequency absorption lines at 31 and 85 cm^{-1}, which appear at higher temperatures. Their oscillator strengths increase quasi-linearly with temperature up to

about $T = 60$ K, this will be discussed in more detail later. The fast fringes between 60 and 90 cm^{-1} are due to the Fabry-Perot interference in the sample.

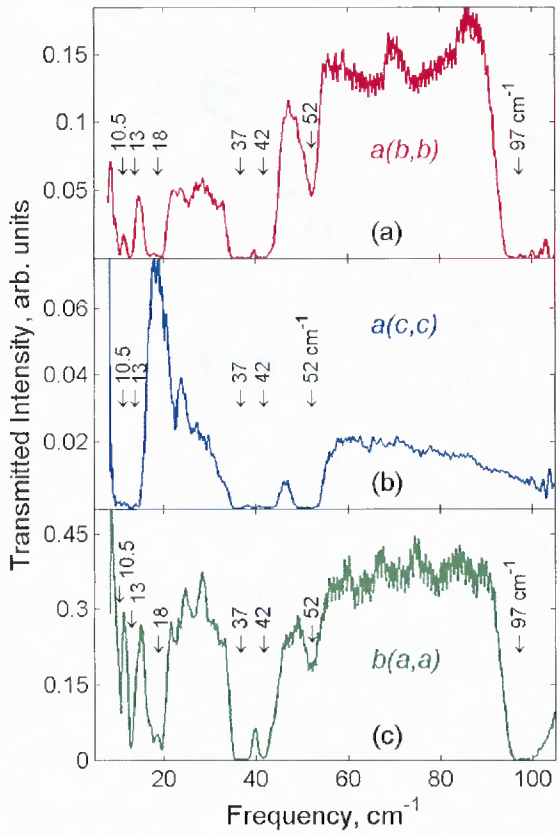

Figure 5.1 (a), (b), (c) Normalized Fourier-transform far-IR transmission spectra of $HoMn_2O_5$ single crystal measured at $T = 5$ K in *a(b,b)*, *a(c,c)*, and *b(a,a)* configurations, respectively. Arrows indicate the frequencies of IR-active absorption lines.

Transmission intensity maps (Figure 5.2) were measured in *a(b,b)*, *b(a,a)*, and *a(c,c)* configurations with temperature increments of 0.5 K in the range of $T < 50$ K and about 5 K at $T > 50$ K. The results for the *a(b,b)* configuration, will be discussed first, where the electric field $\vec{e}$ of both incoming and transmitted light is parallel to the direction of spontaneous electric polarization along *b*-axis. Drastic increase of absorption at 10.5, 13, 18 cm^{-1} and 42 cm^{-1} occurs upon cooling at $T_3 = 19$ K. The primary changes in the IR spectra at the magnetic phase transitions revealed themselves as an increase in

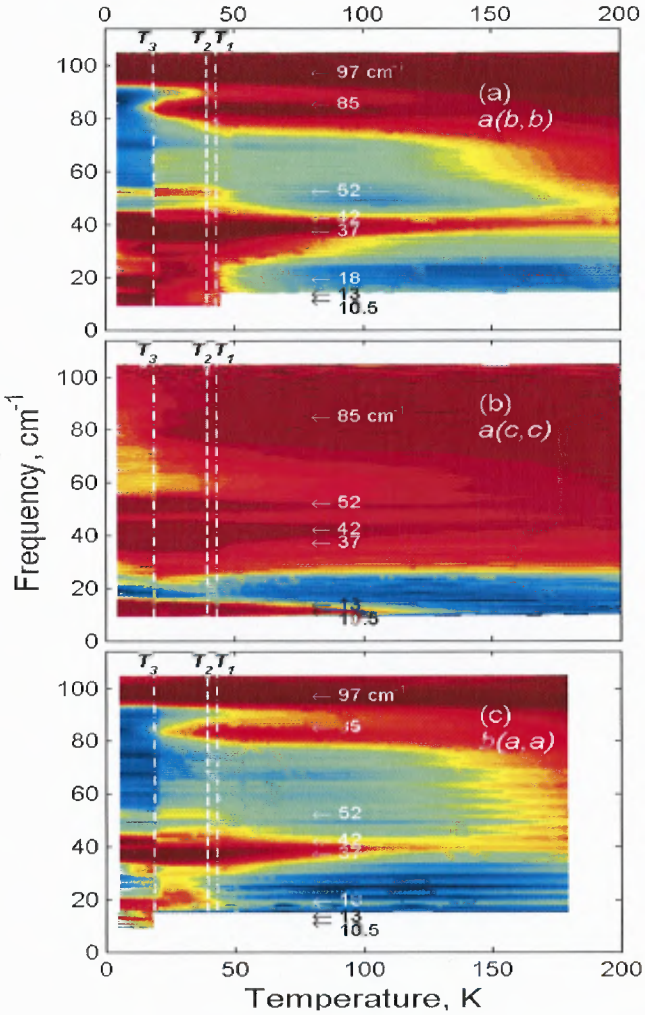

Figure 5.2 Maps of transmitted intensity *vs.* temperature and frequency for $HoMn_2O_5$ in (a) *a(b,b)* , (b) *a(c,c),* and (c) *b(a,a)* configurations. Red (dark) color corresponds to stronger absorption, while blue (light) color indicates high transmission. The scales of the transmission intensity for each plot are the same as that for the corresponding graphs in Figure 5.1.

the oscillator strengths but not as the frequency softening for the transverse oscillators as is usually observed in ferroelectrics, due to the Lyddane-Sachs-Teller relation [61].

The temperature-frequency maps measured for different *z(x,y)* configurations demonstrated a relatively weak dependence on the direction of the light propagation direction z as it is expected for oscillators with a $\vec{k}$-vector ≈ 0. At the same time, absorption spectra of anisotropic $HoMn_2O_5$ crystals depend strongly on the light

polarization with respect to the crystallographic directions. In particular, for the case where the electric field of light perpendicular or parallel to the Mn spin ordering plane: $\vec{e} \parallel c$ and $\vec{e} \perp c$, respectively. For example, in the *a(c,c)* transmission configuration the doublet at 10.5 and 13 cm^{-1} dominates the low-frequency part of the spectrum [see Figure 5.2(b)]. Near the temperature intervals, at $T_2 = 39$ K and $T_1 = 43$ K, the doublet merges to a single line with a frequency of about 12 cm^{-1}, which maintains a significant oscillator strength far above $T_1 = 43$ K in the paramagnetic phase. The 18 cm^{-1} oscillator, which is strong in orthogonal *a(b,b)* and *b(a,a)* configurations, is not optically active for *a(c,c)* transmission in the entire temperature range.

5.5 Fitting of Spectra to Lorentz Model

Transmission spectra were fitted using *SCOUT-2* software based on the Lorentz model for the parametric description of the dielectric function:

$$\varepsilon(\omega) = \varepsilon_\infty + \sum_j^N \frac{S_j \Omega_j^2}{\Omega_j^2 - \omega^2 - i\gamma_j \omega}, \tag{5.1}$$

where Ω_j, S_j, and γ_j are the oscillator's frequency, strength, and damping, respectively. Since the oscillator frequencies Ω_j are practically constant for all excitations in the temperature range $T \leq 70$ K, it is convenient to present the oscillator strength S_j in the same units as that for the static dielectric function by adding $\Omega^2{}_j$ in the numerator of Equation 5.1. Oscillator parameters for the primary absorption lines are summarized in Table 5.1.

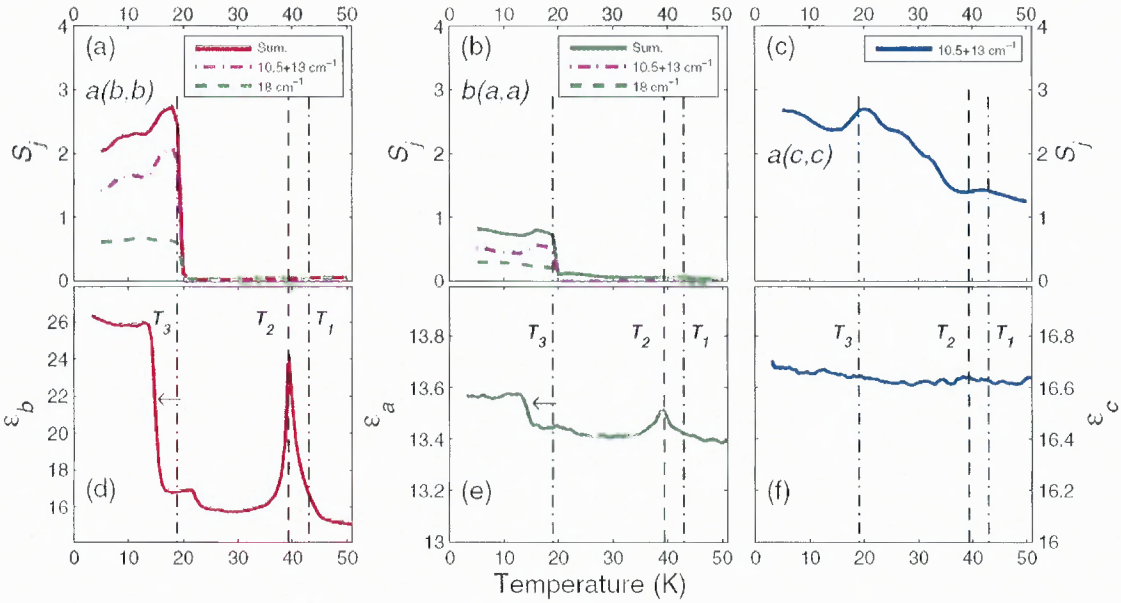

Figure 5.3 (a), (b), and (c) Temperature dependence of the oscillator strength S_j presented in units of the static dielectric function $\varepsilon(0)$ in *a(b,b)*, *b(a,a)*, and *a(c,c)* polarization configurations, respectively. (d), (e), and (f) Temperature dependencies of ε_a, ε_b, and ε_c measured for different orientations of the same $HoMn_2O_5$ crystals. The shift of the T_3 transition temperature between the IR and dielectric measurements is shown with horizontal arrows in (d) and (e).

Figure 5.3 shows a comparison between the static dielectric function $\varepsilon(T)$ and oscillator strengths $S_j(T)$. A quantitative relation in the step-like behavior of the *b*-directional static dielectric function $\varepsilon_b(T)$ at T_3 with the contribution of these particular excitations (see Figure 5.3(a) and References [51,60] for details of dielectric measurements). For the *a(b,b)* polarization, the low-frequency doublet at 10.5 and 13 cm^{-1} provides the strongest contribution of about 2.2 to $\varepsilon_b(T)$ [Figure 5.3(a)]. The 18 cm^{-1} oscillator contributes only about 0.5 at $T < T_3$, which significantly weakens at T_2, and disappears above T_1. The higher frequency line at 37 cm^{-1} maintains oscillator strength of about 0.5 at low temperatures and gradually decreases in the temperature

range up to ~150 K. The difference in the temperature of the incommensurate-commensurate T_3 transition obtained from IR and dielectric measurements [compare Figures 5.3(a) and 5.3(d)], is due to thermal hysteresis. The IR transmission spectra were measured in the warming regime, while dielectric data were taken upon cooling. The quantitative discrepancy between $\Delta\varepsilon(T)$ and $\sum S_j(T)$ at T_3 can be influenced by systematic errors of the experiment, such as oscillator over damping due to the sample thickness and imperfections of linear polarizers. Note that the magnitude of ε_∞ in the parent compound of $TbMn_2O_5$ has been recently related to the contribution of transverse optical phonons [55], which should be the case for $HoMn_2O_5$ crystals as well.

Table 5.1. Polarization, Frequency Ω_j, and Oscillator Strength S_j of the Low-Frequency Ligand Field Optical Transitions in $HoMn_2O_5$.

	Polarization	Ω, cm^{-1}	$< S_j >$ $T = 5-19\,K$	Type	Comments
$HoMn_2O_5$	*a(b,b)*	10.5 and	1.3	ED	Disappears > T_3
		13	0.6	ED+MD	Disappears > T_2
		18		ED+MD	Disappears > 200 K
		37		ED+MD	Weak; Disappears > T_3
		42		MD	
		97			
	b(a,a)	10.5 and	0.5	ED	Disappears > T_3
		13	0.3	ED+MD	Disappears > T_3
		18		ED+MD	Disappears > 150 K
		37		MD	
		97			
	a(c,c) and *b(c,c)*	10.5 and	3	ED	Disappears > 150 K
		13		ED+MD	Disappears > T_2
		37		ED+MD	Disappears > 150 K
		42		ED	Weak
		52			
$TbMn_2O_5$ Ref. [58]	$\vec{e} \parallel b$	9.6	3.6	ED	"electromagnon" Ref. [58]

Note: the units of the oscillator strength S_j are the same as that for the static dielectric function. The type of electric dipole, magnetic dipole, or mixed activity is marked with ED, MD, and ED+MD, respectively.

Higher frequency IR absorption lines do not show significant changes at phase transition temperatures. The broad feature at 97 cm^{-1} is polarized in the *a-b* plane and is not active for light polarization along the *c* axis. A weaker high-frequency absorption peak at 85 cm^{-1} develops at temperatures lower than the commensurate-incommensurate transition T_3 with its oscillator strength increasing quasi-linearly with temperature up to

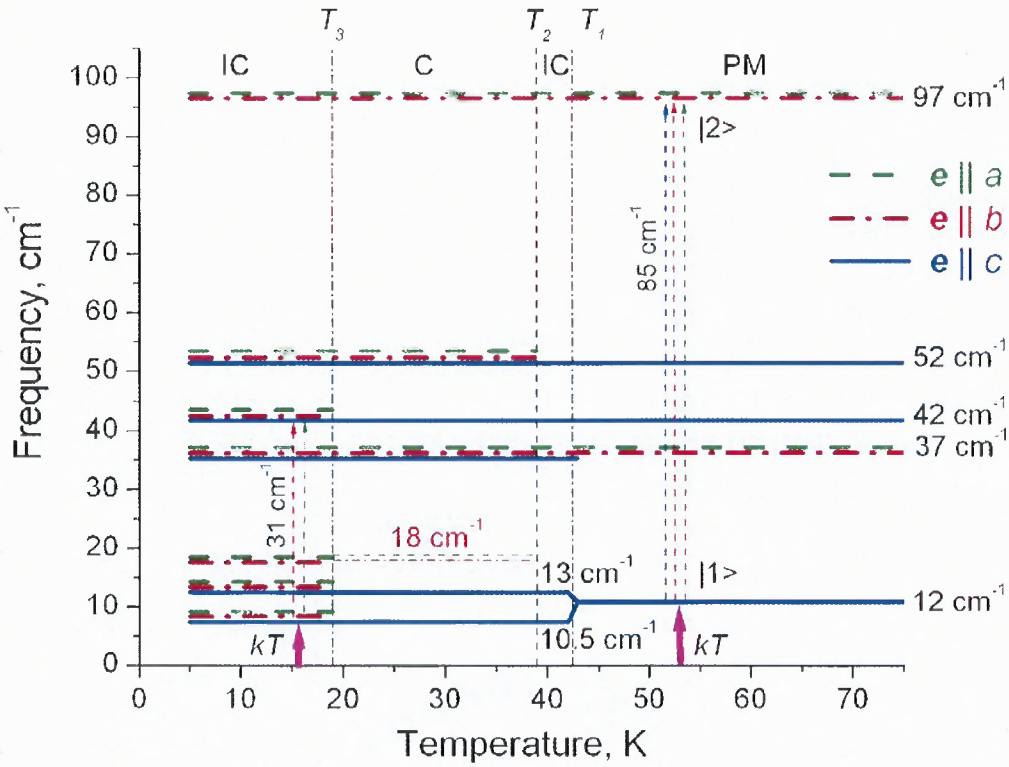

Figure 5.4 Schematics of the energy diagram for optical transitions between ligand field split levels of the Ho^{3+} multiplet ($^5I_8$) in $HoMn_2O_5$. The energies of experimentally observed transitions from the ground state are represented with horizontal lines. Dashed, dash-dot, and solid lines indicate the allowed polarization for the corresponding transitions: *a(b,b)*, *b(a,a)*, and *a(c,c)*, respectively. Short vertical arrows indicate thermal activation from the ground state to the nearest excited state with a consecutive optical transition (31 and 85 cm^{-1}) to the higher energy states. Splitting of the lowest excited state (12 cm^{-1} → 10.5 + 13 cm^{-1}) occurs in the vicinity of T_2 upon cooling. Vertical dash-dot lines divide different magnetic phases: incommensurate AFM (IC), commensurate AFM (C), and paramagnetic (PM).

~60 K. Although its contribution to $\varepsilon(T)$ is negligibly small (below 0.03) compared to that of the lower frequency oscillators, this high-frequency line is important in the interpretation of the observed IR excitations as originating from split LF states of Ho^{3+}. Figure 5.4 depicts schematically nearly all of the observed optical excitations. Dashed, dash-dot, and solid lines correspond to the light polarization along *a*, *b*, and *c* directions, respectively. All observed IR excitations (except the 18 cm^{-1} mode) remain optically active in at least one polarization configuration in the paramagnetic phase, i.e., at the temperatures well above $T_1 \approx 43$ K.

5.6 Split Ligand Field Excitations

The Ho $^{3+}$ ions in $HoMn_2O_5$ contains ten 4*f* electrons. According to Hund's rule, the ground state term for these ten electrons is $^{(2S+1)=5}I_{J=8}$ [62], with $2J+1=17$ degenerate states. The degeneracy of these states is lifted by a reduction of symmetry due to the surrounding Ligand field (LF) perturbations. The ligand field is distinguished from simpler crystal fields, because the effect of the surrounding Mn ions on Ho^{3+} is more complex than a Coulomb potential. The hybridization between 4*f* states of Ho^{3+} and 3*d* states of Mn needs to be accounted for within the Hamiltonian, through the addition of a covalent bonding term. The role of intervening oxygen ions may also need to be considered, such as in the case of a magnetic coupling due to a superexchange from the 2*p* orbitals of the non-magnetic oxygen anions [63], as occurred, for example, in heavy fermions compounds, is expected to give rise to coupling between spin states of Mn ions and ligand field states of Ho ions.

In the case of rare-earth ions, the outer most shells are striped away leaving the filled 5*s* and 5*p* shells behind, which act to partly shield the 4*f* orbitals from the external ligand field. Hence, excitations between Ho^{3+} split states should be significantly less energetic than in the case of transition metal ions where the optically active 3*d* orbitals are the outré-most shell and lay exposed to the external fields. Several neutron scattering studies of related compounds, such as $HoVO_4$ and $HoMnO_3$, provide an estimate for the frequency range of the LF transitions (12 - 300 cm^{-1}) [64,65]. For example, the low-energy dispersionless excitations, which have been attributed to the crystal field splitting of Ho^{3+} in $HoMnO_3$, are at 12 and 25 cm^{-1}. Therefore, the observed $HoMn_2O_5$ infrared excitations can be said to originate, with some possible exceptions, from dipolar transitions between the ground state and the low energy excited LF states within the $J = 8$ multiplet.

Conventional electric dipole optical transitions, for electrons in a centro-symmetric potential, between the levels of the $4f_n$ configuration are all forbidden by the parity rule, i.e., transitions between levels of even parity are forbidden. In contrast, magnetic-dipole transitions are allowed between states of the same parity. The standard angular-momentum method (free ion, LS coupling) gives the selection rules for magnetic dipole transitions, which are independent of the crystal field. Magnetic dipoles are active between states with ΔJ=0,±1, where ΔJ=±1 corresponds to transitions between the neighboring multiplet components with ΔS=0, ΔL=0, and ΔJ=0 and is meaningful in external magnetic field only. Although this is always true for a free ion, the lower symmetry of the LF potential in crystals can result in the appearance of forced electric-dipole transitions in addition to the magnetic-dipole transitions. A forced electric-dipole

transition occurs when Ho^{3+} is placed in a LF that has no center of symmetry, such as in RMn_2O_5 [66,42] Hence, the wave function of Ho^{3+} has a mixed parity. The oscillator strength for the forced electric dipole transition is determined by the admixture of the states with the opposite parity (e.g., *d* electrons) to the predominantly even parity of Ho^{3+} in the 4*f* configuration [58]. Selection rules for the forced electric-dipole transitions depend on the exact symmetry of the LF, and their analysis at the phase transitions in RMn_2O_5 requires separate theoretical studies. It should be mentioned that the selection rules for the forced electric-dipole transitions with $\Delta J=0,\pm1$ requires reversed light polarization (circular σ versus linear π) for the confirmation of magnetic dipole transitions [42,67].

According to the Wigner-Eckart theorem [68], the *z*-direction dipolar transition between two LF states can be non-zero, only if the two states have common J_z components. Similarly, the *x*- or *y*-directional dipolar transitions can be non-zero, only if the two states have J_z components that are different by ± 1. For $HoMn_2O_5$, the *z*-axis was chosen to correspond to the crystalline *c*-axis. Correspondingly, *x*- and *y*-axis are along crystalline *a* and *b* directions. Figure 5.2 shows that the main change at the magnetic ordering temperatures occurs to the polarization of LF transitions. For instance, the IR excitations at 10.5 cm^{-1} and 13 cm^{-1} are present only for the incident light polarized along *c* direction and are absent for the incident light polarized along *a* and *b* directions for the temperature range above T_3. This means that the ground state and the excited states at 10.5 cm^{-1} and 13 cm^{-1} share the same J_z components, but do not have any J_z components separated by ± 1; therefore they do not cancel the contribution to the dipole transition matrix element. The appearance of IR excitations at 10.5 cm^{-1} and 13 cm^{-1}

polarized along a and b axes below T_3 can be interpreted as a symmetry change of either the ground state or the excited state in such a way that the ground and the excited states have uncompensated J_z components separated by ± 1. Such changes can occur, for example, through the mixing with another low energy state, which can be excited from the ground state by a and b polarizations above T_3, such as the one at 37 cm^{-1}.

Modification in the ligand field, which causes such mixing of electron states below T_3, is due to the commensurate-to-incommensurate AFM phase transition for Mn spins. Since the primary cause of the Ho^{3+} LF splitting is still the electrostatic potential from the surrounding ions, i.e., the crystal field effect, the energy spectrum of the LF states is determined by the electrostatic interaction within the crystal lattice. This energy scale stays practically unchanged in a wide temperature range. However, magnetic effects at $T < T_1$, which appear due to the mixing (or covalent bonding) of Ho^{3+} $4f$ states with the ordered spins of the nearest neighbor Mn $3d$ states, influences the symmetry of LF states; which can change at each magnetic ordering temperature resulting in transformation of the selection rules for the corresponding optical transitions. The weak nature of $4f$–$3d$ mixing does not allow significant shifts of the level energy, but affects (in the first order of the perturbation theory) the selection rules for optical transitions. Thus, the results imply that one of the main causes of the sudden steps in the dielectric constant along a and b directions at T_3 is the coupling between the magnetism on the Mn sub-lattice and Ho^{3+} LF states. The similar energy scale between magnetic interaction and LF splitting supports the importance of the LF splitting and connects the magnetism and dielectric properties of the multiferroic $HoMn_2O_5$ and, perhaps in other related RMn_2O_5 compounds.

5.7 Magnon – Ligand Field Coupling

In addition to the coupling between R^{3+} LF states and the magnetism on the Mn sublattice, of special interest are the symmetry changes due to magnetically induced lattice modulation and dynamic interactions with the lattice. The latter is especially important for the case when the high-energy LF states are in resonance with the lower-frequency IR-active TO phonons (150 cm^{-1}); however, this mechanism should not have any strong temperature dependence. In contrast, the influence of magnetostriction on the change in selection rules for the LF transitions can result in anomalies at the phase transitions. However, the strongest changes in the lattice distortion for RMn_2O_5 compounds are usually observed between T_3 and T_1 [69]. Since the change in selection rules for the LF transitions occurs for $T<T_3$, it supplies a supporting argument for the interpretation of a coupling between the magnetism on the Mn sublattice and Ho^{3+} LF states. The splitting of the 12 cm^{-1} state into a doublet (10.5 and 13 cm^{-1}) at $T_C = T_2 = 39$ K can be attributed to the symmetry lowering, which is caused by electric polarization.

The coupling between Mn spin and Ho^{3+} LF states opens the possibility of composite excitations of magnon and LF states in this compound, which are particularly due to their similar energy scale. The two main criteria for identification of such composite excitations should be (i) their activity occurs only in the temperature range below T_1 and (ii) a nonzero dispersion, which is typical for AFM magnons. Can we identify such excitations in our spectra for $HoMn_2O_5$? The only candidate for the composite LF magnon is the peak at 18 cm^{-1} which is close to the LF transitions at 10.5 and 13 cm^{-1}. This peak dominates in the (*b, b*) polarization below T_3 and maintains sufficient strength above T_3, but is absent for all polarizations above T_1; thus, satisfying

the first criterion for electric-dipole active LF-magnon excitations. But since the second criterion cannot be verified with the IR transmission technique, our interpretation requires additional experimental proofs, which can be obtained, for example, using neutron scattering. Thus, the question whether the IR transition at 18 cm^{-1} is a composite LF-magnon excitation or just another LF state, which became electric-dipole active due to the symmetry change below T_1, remains open. In any case, however, we emphasize that the oscillator strength of the excitation at 18 cm^{-1} is only 20% of the combined oscillator strength for the low frequency LF doublet at 10.5 and 13 cm^{-1}, thus, making this proposed LF magnon to be of secondary importance for explanation of the step-like behavior of the static dielectric function. Appearance of this excitation in (a, a) polarization with a significantly lower oscillator strength can be interpreted as due to a mixed electric- and magnetic-dipole activities of this excitation.

5.8 Thermally Excited Transitions

Thermally excited LF states exist at 31, 80, and 85 cm^{-1}. The temperature-activated transitions at 31 and 85 cm^{-1} are marked with arrows in Figure 5.5(a), which compare two transmission spectra measured at T=5 and 18 K. The absorption peak at 85 cm^{-1} appears below T_3 and becomes stronger as the temperature increases. This IR excitation can be considered as the optical transition from the lowest excited LF state (the doublet at 10.5 and 13 cm^{-1}) to the higher-energy LF state at 97 cm^{-1}. Similarly, the 31 cm^{-1} excitation below T_3 can be considered as the excitation from the same thermally excited LF state to the 42 cm−1 excited state. These thermally excited excitations can be found in the temperature-frequency maps in Figure 5.2, and they are also indicated in Figure 5.5(a)

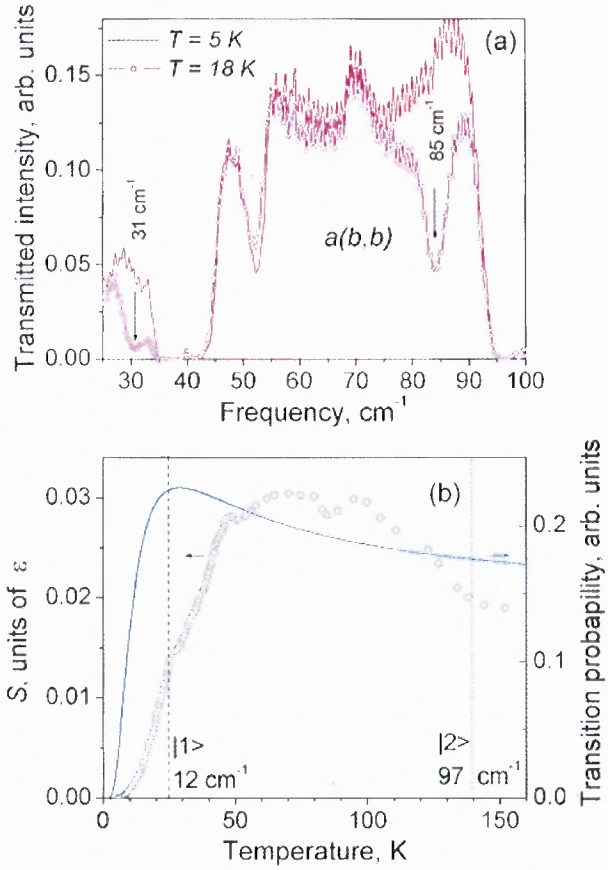

Figure 5.5 (a) Normalized Fourier-transform far-IR transmission spectra of a $HoMn_2O_5$ single crystal measured at $T = 5$ K and 18 K in *a(b,b)* configurations. Arrows indicate the frequencies of the temperature-activated optical transitions at 31 and 85 cm^{-1}. (b) Temperature dependence of the oscillator strength for 85 cm^{-1} transition (circles) is presented in the units of the static dielectric function (left scale). Solid curve (right scale) shows the expected trend for the probability of the temperature-activated transition between two excited LF states, $|1\rangle$ at 12 and $|2\rangle$ at 97 cm^{-1}, which was calculated in a simplified model for a 6-level system.

with dashed vertical arrows. For the thermally activated transitions between two excited LF states, $|1\rangle$ and $|2\rangle$, one can expect that the transition probability $W_{|1\rangle\to|2\rangle}$ depends on temperature activated occupation of the $|1\rangle$ excited state. At low temperatures, this dependence is dominated by the quasi-linear in T term, while at higher temperatures (above 60 K for 85 cm^{-1} transition), depopulation of the ground state to other excited states results in a slow decrease in transition probability. Figure 5.5(b) compares the

probability of the thermally activated transitions $W_{|1\rangle\to|2\rangle}$, which has been calculated in a simplified six-level model, with experimental data for the oscillator strength of 85 cm^{-1} excitation. Exact calculations should take into account the position and wave-function symmetry for all $4f$ Ho^{3+} states, which should give a better agreement with experiment. Our IR transmission spectra did not reveal any sharp variations at $T_C = T_2$, and we cannot assign any specific oscillator that changes its strength or frequency, explaining the spike in $\varepsilon(T)$ at T_2 as shown in Figures. 5.3(d) and 5.3(e). The corresponding feature of the static dielectric function in $TbMn_2O_5$ was explained in Reference [58] by the zero-frequency electromagnon mode. This peak is possibly related to the spontaneous electric polarization due to the ferroelectric domain structure.

5.9 Electromagnons

The FIR transmission spectra in RMn_2O_5 compounds vary for different elements, such as Tb, Dy, and Ho. Both the lowest IR transition frequency and the higher-frequency absorption peaks change for different compounds by a few cm^{-1}. Table 5.1 includes frequencies of LF transitions in $HoMn_2O_5$ along with the lowest optical transition frequency in $TbMn_2O_5$, which was attributed to an electromagnon in Reference [58]. In contrast to the transmission results for $TbMn_2O_5$ with a strong electromagnon mode at 9.6 cm^{-1} polarized along b axis, in $HoMn_2O_5$ we have observed a LF doublet at 10.5 and 13 cm^{-1}. As was described above, this transition is IR active in both $a(c,c)$ and $a(b,b)$ configurations that are preferably polarized perpendicular to the direction of spontaneous polarization b with the polarization degree of $(S^{a(c,c)} - S^{a(b,b)})/(S^{a(c,c)} + S^{a(b,b)}) = 0.4$.

Here $S^{a(c,c)}$ and $S^{a(b,b)}$ are the oscillator strengths from Table 5.1 for $a(c,c)$ and $a(b,b)$ configurations, respectively.

The electromagnon is a new composite excitation recently proposed for RMnO$_3$ (R=Gd and Tb, Reference [38]) and RMn$_2$O$_5$ (R=Y and Tb) [58]. The origin of electric-dipole activity for this excitation with a typical frequency between 10 and 20 cm^{-1} was attributed in Reference [57] and [58] to the interaction with optical phonons. In spite of the strong spin-lattice coupling in these multiferroic compounds, it is still under debate whether the two excitations, separated by a large energy scale (optical phonon having usually one order of magnitude larger energy than electromagnons), could experience a direct coupling, which is strong enough to explain the magnetoelectric effect. In compounds such as RMn$_2$O$_5$ and RMnO$_3$ with R=Gd, Tb, Dy, and Ho (rare-earth ions with f electrons), it might be more fruitful to consider composite excitations between magnons and forced electric dipole LF excitations since they have a more comparable energy scales. In a general case, dynamic interactions between the lattice and magnons can be mediated by the LF states, which have resonances in both magnon and phonon spectral ranges. For other multiferroic compounds with rare earth ions without nominal f electrons, the physics can be even more versatile and the concept of electromagnons could be more valuable, especially in the case of YMn$_2$O$_5$ compound [58] with a direct $3d$-$3d$ interaction.

5.10 Conclusion

Results of the linearly-polarized FIR spectra demonstrated the strong influence of the ligand field between Ho^{3+} and Mn spin states on IR transmission properties of $HoMn_2O_5$. This coupling can explain the step-like anomalies in the dielectric constant in RMn_2O_5 compounds with rare-earth ions having incomplete 4*f*-shell. Further magneto-optical and neutron spectroscopy experiments are required to confirm the existence of LF-magnon composite excitations.

CHAPTER 6

SELF-ASSEMBLED ARRANGMENT OF $ZnMnGaO_4$ NANO-RODS

The following Chapter details the use of synchrotron radiation-based reciprocal space mapping (RSM) to investigate the complex structural properties of epitaxially grown $ZnMnGaO_4$ thin films on single crystal MgO (001) substrates. The $ZnMnGaO_4$ films consist of a self-assembled checker board (CB) structure of highly aligned and regularly spaced vertical nano-rods. The formation is driven by a strain accommodating interaction between Jahn-Teller (JT) active and inactive regions. Lattice parameters of the CB structure were analyzed using H-K, H-L, and K-L cross-sectional reciprocal space mapping (RSM) for various symmetric and asymmetric reflections. The maps revealed a CB structure consisting of two perpendicularly oriented orthorhombic and two conversely twisted tetragonal domains with accommodating atomic displacements at the domain wall interfaces.

Portions of this work have been published in:

- S. M. O'Malley, P. L. Bonanno, K. H. Ahn, and A. A. Sirenko, A. Kazimirov, S. Park and S-W. Cheong, Epitaxial checkerboard arrangement of nanorods in "$ZnMnGaO_4$ films studied by x-ray diffraction," Phys. Rev. B **78**, 165425 (2008).
- S. Park, Y. Horiba, T. Asada, L. S. Wielunski, N. lee, P. L. Bananno, S. M. O'Malley, A. A. Sirenko, A. Kazimirov, M. Tanimura, T. Gustafsson, and S.-W. Cheong, "Highly aligned epitaxial nanorods with a checkerboard pattern in oxide films", Nano Letters **8**, 720 (2008).

6.1 Overview of Growth

The ternary oxide parent compound can be consideration as composed of admixture of the two binary oxides: $ZnGa_2O_4$ and $ZnMn_2O_4$. The cubic $ZnGa_2O_4$ has gained interest

itself as a potential semiconductor material with its ~1.23 eV optical gap, while $ZnMn_2O_4$ (which is cubic at high temperature, but below ~1323 K becomes tetragonal) is essentially insulating with a bandgap of 4.1 eV. The nano-checkerboard structure of $ZnMnGaO_4$ was first observed in bulk polycrystalline samples prepared by the conventional solid state reaction method in air [20]. The current state of understanding for the self-assembled CB formation of ZMGO is that it occurs during the annealing process: where upon cooling the high temperature cubic phase experiences a Jahn-Teller (JT) phase transition to a lower symmetry tetragonal phase. The spinel structure of $ZnMnGaO_4$ is characteristic of ceramic XY_2O_4 compounds. A normal spinel would ideally be coordinated with *X* cations at the tetrahedral (*A*) and *Y* cations at the octahedral (*B*) lattice sites. During the solid-phase growth, the initial high temperature phase contains an equal mixture of Mn^{3+} and Ga^{3+} ions occupying both the *A* and *B* sites. In the complex the manganese atoms are stripped of their two *4s* and one *3d* electrons, leaving behind a Mn^{3+} cation with a partially filled *d*-orbital. When these Mn ions occupy the *B* octahedral lattice sites, the surrounding ligand field will perturb the z-axis component of the outermost electrons in this case the *d*-orbitals and, hence, remove the electronic degeneracy ground state by means of an structural distortion. This effect is what is known as the Jahn-Teller effect and the distortion typically involves an elongation of the bonds along the z-direction. The distortions from JT-active Mn^{3+} ions causes the structural cubic-tetragonal transition, which occurs in the early stages of annealing. The combination of JT-active and -inactive ions induces a miscibility gap within the system of mixed ions. Subsequently, diffusionless spinoidal decomposition precipitates into two equilibrium phases with chemical compositions close to the miscibility gap boundaries.

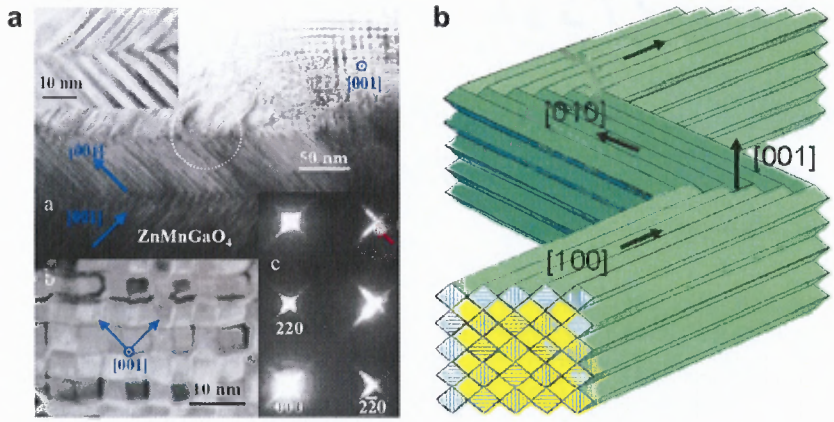

Figure 6.1 (a) Set of TEM images of bulk $ZnGaMnO_4$ depicting the checkerboard and herringbone structural formation (b) illustration depicting two compositional different nano-rod domains in an arrangement analogous to that found in bulk ZMGO [72].

The last stage in the CB formation is a diffusion process of the mixture into spatially separate Mn-rich and Mn–poor regions. The driving force behind this is the aggregative nature of the JT active ions. The system coarsens into alternating Mn-rich (tetragonal) and Mn-poor (cubic) regions while coexisting by forming a strain-accommodating CB structure [20,22,23,70,71,72]. The unique aspect of this bulk material is its self-assembled formation of alternating nano-rod like domains to form a in-pnlane checkerboard-type structure accompanied by an out-plane herringbone (HB) structure. The arrangement is shown in Figure 6.1a by the TEM images and illustratively in Figure 6.1b. An important step towards utilization of this intriguing phenomenon for large-scale planar device technology is the epitaxial growth of thin CB films [24]. Such a planar CB surface could be utilized as a template for the subsequent growth of ferromagnetic material and the construction of high density magnetic recording devices.

6.2 Sample Growth and Description

The thin film ZMGO samples used in the subsequent x-ray diffraction studies were grown by pulsed laser deposition (PLD) by the research team at Rutgers Center for Emergent Materials. The PLD growth technique can be summarized using the schematic in Figure 6.2 where the beam from a high power pulsed laser is steered into an ultra high vacuum (UHV) chamber and focused onto a target material. The material absorbs the incoming electromagnetic energy and subsequently ablates a small volume of material ejecting from the surface. The material travels in the direction of a heated substrate where growth/deposition can occur.

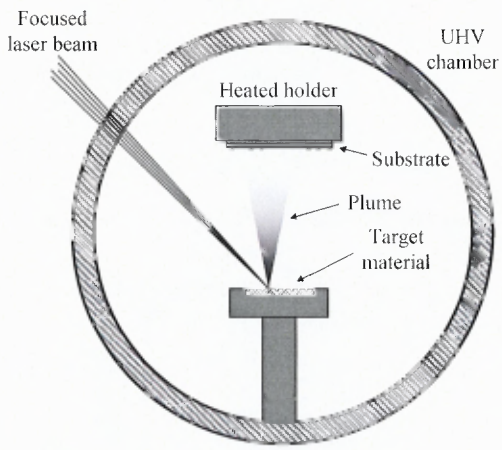

Figure 6.2 Schematic of a pulsed laser deposition (PLD) configuration.

The sample used in this study was grown using a homogenous high-temperature quenched form of ZMGO, with tetragonal lattice (a = 0.82 nm, c = 0.87 nm), as the target material along with a KF excimer laser. The substrate was single crystal cubic MgO (001) with lattice constant a = 0.4212 nm. The CB patterned epilayer is formed of two periodically alternating and structurally different spinel phases: (i) Mn-poor, JT inactive and (ii) Mn-rich, JT-active. From TEM imaging of the sample (Figure 2.6) the

typical size of a single domain within the CB structure was determined to be 4×4×750 nm^3 and are highly aligned along the <001> growth direction. A significant number of ZMGO films have been grown, which show consistency in the formation of a checkerboard structure.

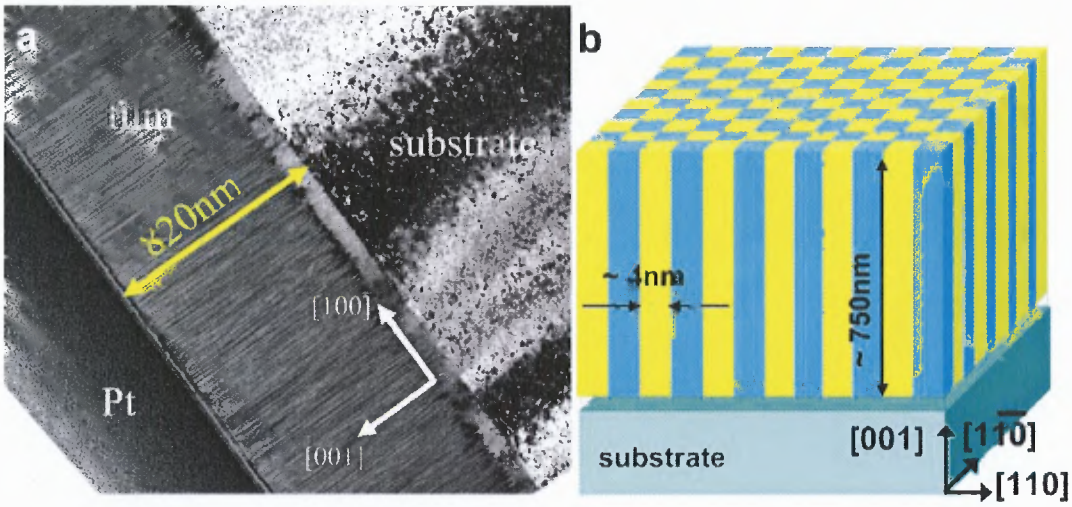

Figure 6.3 (a) Cross-sectional TEM image of the ZMGO film. (b) Illustration of CB structure showing the in-plane CB argument of vertical aligned 4x4x750 nm^3 nano-rod domains [24].

6.3 Measurement Parameters

Reciprocal space mapping (RSM) were carried out at the A2 beamline of Cornell High Energy Synchrotron Source (CHESS). The high brilliance and large photon flux densities characteristic of synchrotron sources were beneficial in shortening the otherwise lengthy measurement of reciprocal space maps and in detection of weak diffraction signals. The incident x-ray beam was conditioned using a double-bounce Si (111) monochromator passing photons with an energy of 10.53 keV (λ=1.17745 Å). High angular resolution was achieved by conditioning the scattered beam using a single-bounce Si (111) analyzer crystal. Reciprocal space mapping of the CB structures was measured for several

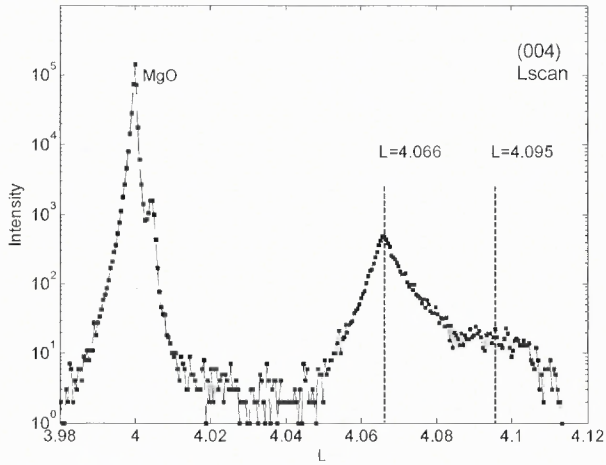

Figure 6.4 L-scan for the symmetric (004) reflection. The largest peak is from the MgO substrate and the two dashed lines mark the location of the CB (L=4.066) and transitional layer (L=4.095) peaks.

symmetric and asymmetric reflections: (002), (-202), (-2-22), (004), (044), (-226). In the following maps the Miller index L corresponds to the film growth direction, while H and K represent the in-plane parameters of the structure. The integer values of H, K, and L correspond to the reciprocal lattice points (RLP) of a cubic spinel structure with lattice parameter a_S = 0.8424 nm (i.e., twice the value of cubic MgO substrate). In this notation the strong (022) diffraction peak of MgO substrate will coincide with the (044) reciprocal lattice point (RLP) of the reference spinel structure.

6.4 Reciprocal Space Maps

The out-plane strain state of the CB epilayer with respect to the underlying MgO substrate was determined by performing a longitudinal L-scan using the symmetric (004) reflection (note: this is analogous to a q_z and ω-2θ scan). The scan is depicted in Figure 6.4, where three diffraction peaks are clearly present: the strong MgO substrate peak at L=4 and two (tensile strained) layer peaks at L=4.066 and 4.095. Note the shoulder

present on the substrate peak is most likely due to distortion of the MgO lattice in the vicinity of the substrate-layer interface. Determining the nature of these peaks required the measurement of several symmetric and asymmetric reciprocal space maps. Figure 6.5 depicts an in-plane H-K RSM of the asymmetric (044) reflection measured at the first layer peak (L=4.07). The cross-sectional map is dominated by several diffraction peaks associated with different structural phases within the film. The central peak labeled *A* can then be said to be elastically strained phase, since it coincides with the (044) RLP and therefore, contains the same in-plane lattice constants as the MgO substrate. Though another asymmetric reflection with H non-zero is needed to confirm this initial assumption. The determination of the in-plane lattice parameters can only be made for corresponding non-zero reflection indices. Hence, the (044) RSM is only sensitive to in-

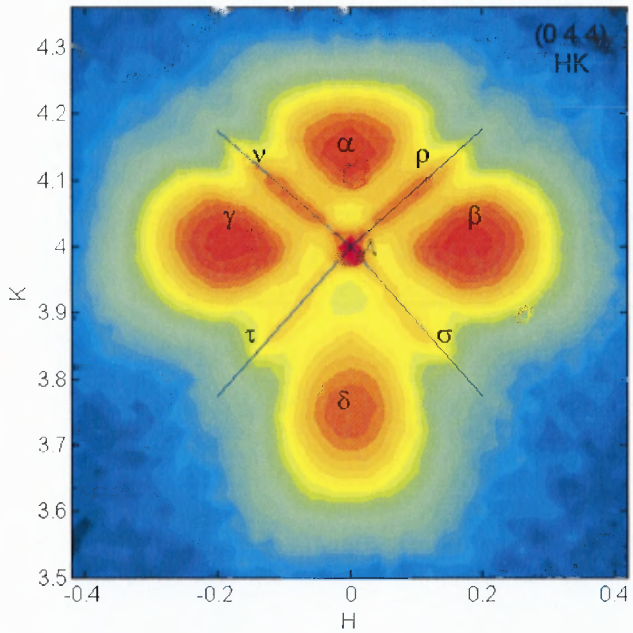

Figure 6.5 Cross-sectional H-K RSM measured around the asymmetric (044) RLP. The α and δ peaks are orthorhombic phases, while the β and γ peaks are rotated tetragonal phases associated with the CB structure. The elastically strained tetragonal phase is labeled *A*. Signal originating from domain boundaries, highlighted by the radial lines emanating from the central (044) RLP, are labeled ρ, σ, τ and υ.

plane lattice spacing along the K direction corresponding, in this case, to the b-axis. The two broad peaks β and γ are practically lattice matched to the substrate with $b_{\beta,\gamma}$ = 0.841 nm, however these phases contain a twist of ±2.55° of their unit cell. This is demonstrated by the displacement along the dashed arc in Figure 6.5, which represents a rotation about the (00L) reciprocal lattice vector. The specific location of the phases along this arc signifies the presence of a discreet twist of the unit cell, in contrast to broadening due to mosaic spread. The two α and δ peaks displaced along the nonzero K direction are inelastically strained. Bear in mind, that in reciprocal space a positive displacement from the referenced (044) RLP represents a decrease in the lattice spacing and conversely a negative displacement is an increase of the corresponding lattice parameter. The peaks α and δ, hence, have short and long in-plane lattice parameters b_α = 0.814 nm and b_δ = 0.898 nm, respectively. The four diagonal peaks ρ, σ, τ, υ have been associated with distortions originating from domain boundaries and will be discussed in detail later.

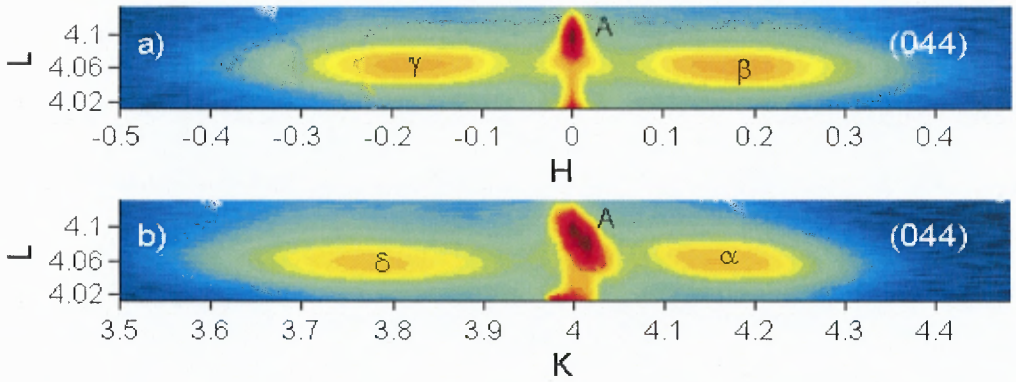

Figure 6.6 (a) H-L and (b) K-L RSM around the (044) RLP. The two lobe shaped peaks in each map correspond to phases within the CB structure. The narrow central peak has been attributed to a layer at the CB/MgO interface.

The inclusion of the two asymmetric H-L and K-L maps, in Figure 6.6, allowed for assignment of the in-plane phases observed in Figure 6.5 to the layer peaks observed in the longitudinal L-scan (Figure 6.4). The elastically strained phase *A* observed in the H-K map can now be related to the broad layer peak in Figure 6.6 at L=4.095, originating from a tetragonal phase with lattice parameters (a_A=0.842 nm, c_A=0.823 nm). The prominent layer peak at L=4.066 can then be attributed to the four broad phases (α, β, γ, and δ) in the asymmetric H-K maps. This observation indicated that these four phases all contain the same out-plane lattice parameter ($c_{\alpha,\beta,\gamma,\delta}$ = 0.829 nm), which is a crucial aspect for their coexistence within the same film volume. It should be noted that this value is close to that of bulk polycrystalline ZMGO [20]. Cross-section transmission electron microscopy (TEM) imaging (Figure 6.7) revealed that the sample film contains a homogeneous transitional layer separating the MgO substrate from the nano-rod checkerboard layer. The layer thicknesses were measured at 735 nm and 85 nm, for CB and transitional layers, respectively.

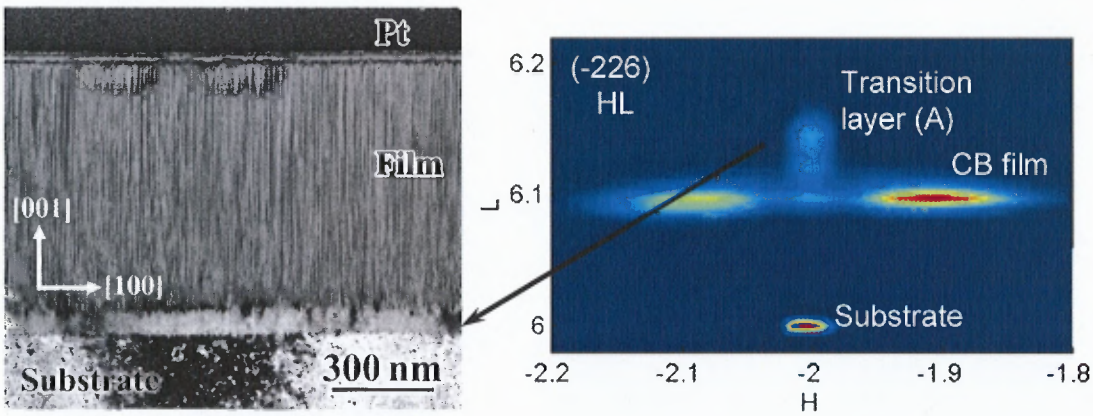

Figure 6.7 Cross-sectional TEM image of the ZMGO sample along side a (-226) RSM. Black arrow points to the corresponding transitional region within the TEM image that is associated with diffraction peak (*A*).

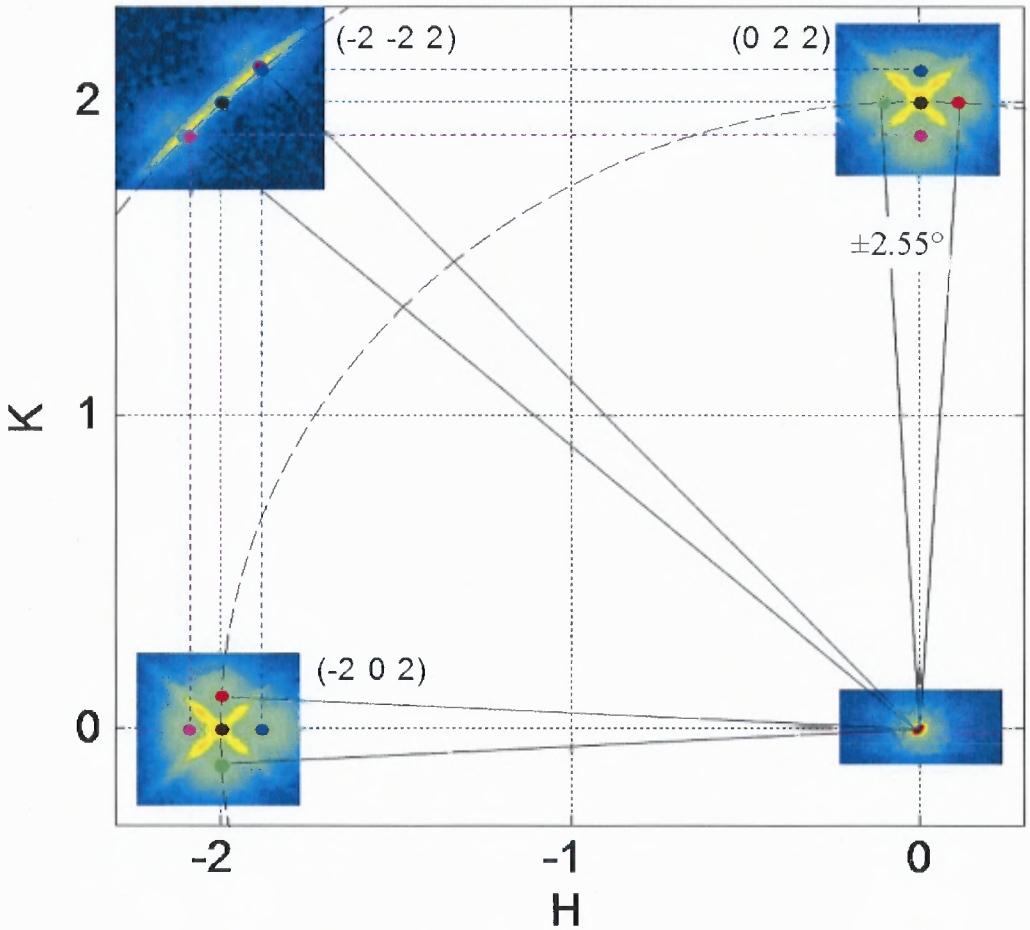

Figure 6.8 Combined plot of the four complimentary (-2-22), (022), (-202), and (004) RSM. Dots represent stimulated peak positions of the unit cell phases within the film. Short dashed lines represent lines of projection between reflection.

The diffraction peak intensity of the structural phases were integrated over their volume in reciprocal space in order to determine the prevalence of each phase within the film. Given the similar out-plane lattice parameters of the four (α, β, γ, and δ) phases their intensity volumes were summed and found to be ~6 times that of the central tetragonal phase (*A*). This ratio is consistent with the relative layer thickness between the CB and transitional regions, as determined by TEM. Comparison of the relative diffracted intensity along with similarities in the out-plane strain state supports the assumption that

peak *A* originates from the thin transition layer and the four (α, β, γ, and δ) phases stem from the novel CB layer, see Figure 6.7.

In order to gain further insight into structural properties of the CB film a series of complementary reflections were measured. Figure 6.8 contains a plot of several HK maps measured around the (-2-22) , (022), (-202) and (004) RLP. The L value was set so that the maps were centered at the middle of the CB peaks. A comparison between the asymmetric skew [(022), (-202)] and symmetric (004) maps revealed that the CB associated peaks have collapsed into a single peak centered at H=K=0. This result is important since it rules out the existence of any discreet tilting of the CB arranged nanorods. *Note*: if the displacement of the tetragonal (β and γ) phases had been from a discreet tilt of the (001) plane instead of the aforementioned twist distortion, the diffraction peaks would have appeared in the same position for both the (044) and (004) RSM. The similarity between the (-202) and (022) reflections signifies a 90° rotational invariance (with translation) of the entire CB structure. In the (-2-22) reflection the peaks for all phases are closely aligned to the arc with a constant magnitude of the reciprocal lattice vector with the radius of $R = 2\sqrt{2}$, shown by the dashed line in Figure 6.7. This observation corresponds to a close proximity of the average in-plane lattice parameter for all α, β, γ, and δ phases to that of the reference spinel structure. Therefore, the average in-plane parameter of the CB structure matches that of the MgO lattice. The colored dots represent a construct of the diffraction patterns by converting the initial assumptions of the unit cell parameters, for each phase, from real into reciprocal space, using Equation 6.1:

$$\vec{b}_1 = \frac{\vec{a}_2 \times \vec{a}_3}{\vec{a}_1 \bullet \vec{a}_2 \times \vec{a}_3}, \vec{b}_2 = \frac{\vec{a}_3 \times \vec{a}_1}{\vec{a}_1 \bullet \vec{a}_2 \times \vec{a}_3}, \vec{b}_3 = \frac{\vec{a}_1 \times \vec{a}_2}{\vec{a}_1 \bullet \vec{a}_2 \times \vec{a}_3} \tag{6.1}$$

Where $\vec{a}_i$ and $\vec{b}_i$ defines the crystal axes in real and reciprocal space, respectively. To locate the peak position in the RSM (in the MgO reference frame) the vector dot product needs to be taken between $\vec{b}_i$ and the reciprocal lattice vector of each reflection. The phase locations can then be traced to confirm the RSM pattern formation of each reflection. Tracing the movement of the α (blue) and δ (pink) phases from the (022) to (-202) RLPs, one can observe that their relative locations within the diffraction pattern flip. By doing so, the crystal phases are formed by two orthorhombic unit cells with long- and short-sides orthogonal to each other. Figure 6.9 summarizes the unit cell lattice parameters for each of the checkerboard associated diffraction peak phases.

The CB epilayer therefore, contains four structurally different spinel phases: two conversely rotated tetragonal (Mn-poor, JT inactive) and two orthogonally oriented

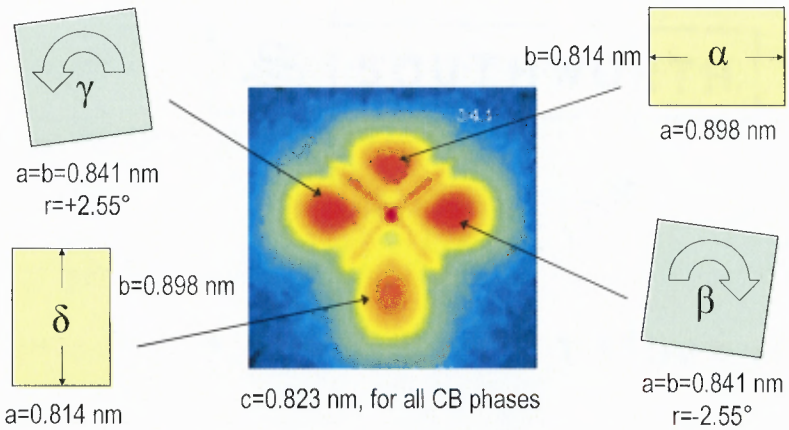

Figure 6.9 Illustration of the four structural unit cell phases present with the CB layer with arrows pointing to the appearance with the asymmetric (044) RSM.

orthorhombic (Mn-rich, JT-active) phases. Each 4×4×750 nm^3 nano-rod domain is then formed by one of these four distorted unit cell phases as depicted in Figure 6.10. The dashed lines define the CB super-cell, which through translational operations can produce the entire CB film. The orthorhombic and rotated tetragonal phases are separated by the domain boundaries (DB) closely aligned along the <110> and <1-10> directions as shown in Figure 6.11. These domain walls should accommodate structural distortions between α, β, γ, and δ phases providing means for their coherence along both the film growth direction and in-plane direction. Cross-sectional RSM were measured around the (-2 0 2) RLP in both the K–L and Π-L planes, Figures 6.11(a) and (b) respectively, where $\Pi=(H+K)/\sqrt{2}$. These maps demonstrate that the out-plane lattice parameters for ρ, σ, τ and υ are the same as that for the α, β, γ, and δ phases, as expected for coherent DB.

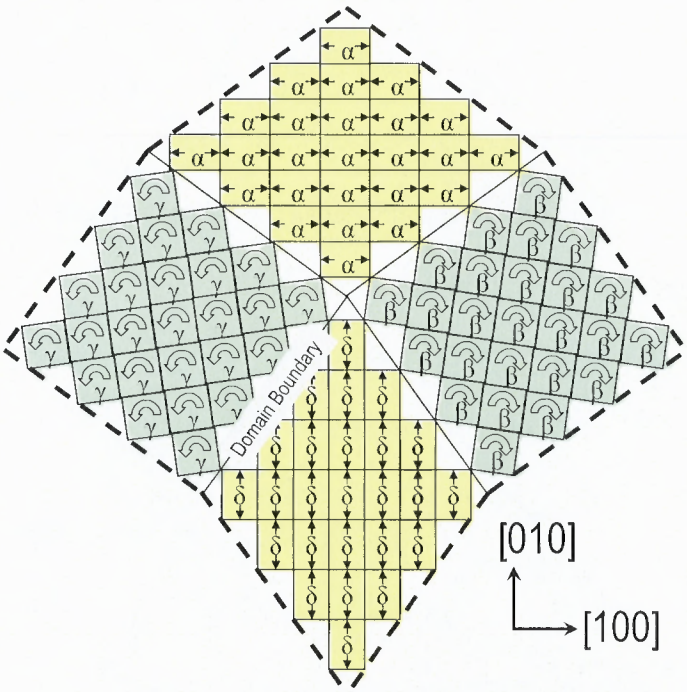

Figure 6.10 Illustration of the CB arrangement of tetragonal and orthorhombic domains with DB along the <110> and <1-10> directions. The dashed lines define the CB super-cell (SC) by which translational operations can repeat the entire CB film.

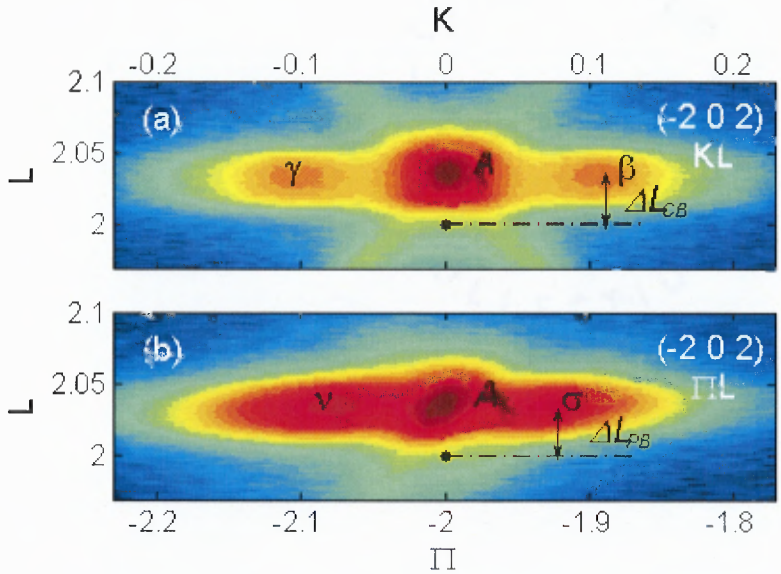

Figure 6.11 (a) K–L and (b) Π-L cross sectional map of the reciprocal space around the (-202) RLP, where Π is in the direction (H+K)/√2, passing throw the υ-σ DB peaks. The black dot signifies the position for the forbidden MgO substrate peak.

6.5 Lateral Correlation Length

The full width at half maximum (FWHM) values in the H–K plane were determined and used to establish the in-plane correlation length of the CB film. Contributions due to coherent domain size on the peak breadth were decoupled from tilt and twist induced inhomogeneous variations of the unit cells. Both the (0 2 2) and (0 4 4) reflections, which belong to the same family of crystallographic planes, were utilized (see Reference [31] for details). The in-plane correlation length D_{H-K} for the CB domains has been estimated to be about $D_{H-K} \approx 25$ nm, where $D_{H-K} = a_s / \xi$, and ξ is the reflection-order-independent component of the peak's breadth. The H–L and K–L maps show the CB peak breadths remain parallel to the sample surface and hence are dominated by size effects. Note that $D_{H-K} \approx 25$ nm is significantly larger than the typical size of the CB

square of ~ 4×4 nm^2 (see TEM in Reference [24]). In the L direction, where inhomogeneous broadening is due to composition fluctuations and film thickness in the growth direction should dominant the peak breadth. The corresponding FWHM is significantly narrower ($FWHM_L$=0.03) compared to the in-plane value. Compositional fluctuations are therefore believed to be relatively well controlled throughout the film. Contributions due to film thickness in the peak breadth can be considered negligible, as a result of the film thickness in the growth direction. A summary of the structural parameters of the CB film can be found in Table 6.1. The strain parameters are presented in terms of the Miller index mismatch.

Table 6.1 Average lattice parameters and related H-K-L values of the different phases within the CB film as Determined From Multiple Reflections.

	$ZnMnGaO_4$ [23] (bulk, *I*41/*amd*)	*A* (transitional)	α / δ (orthorhombic)	β, γ (rotated tetr.)
ΔH/H	—	0.00	–0.03 / 0.04	0.00
ΔK/K	—	0.00	0.04 / –0.03	0.00
ΔL/L	—	0.023	0.016	0.016
a, nm	0.82	0.8424	0.898 / 0.814	0.841
b, nm	0.82	0.8424	0.814 / 0.898	0.841
c, nm	0.87	0.823	0.829	0.829
V/V_s	–0.022	–0.023	+0.013	–0.020
$FWHM_{H-K}$ (0 4 4)	—	0.01	0.13	0.13
$FWHM_L$ (0 4 4)	—	0.02	0.03	0.03
Rotation <0 0 L>	—	0.00	0.00	±2.55°

Note: The lattice and volume mismatch for different phases is normalized to that for the reference spinel structure with a_s = 0.8424 nm.

6.6 Domain Boundary Atomic Distortions

Comparison of the in-plane domain size (4×4 nm^2) and the in-plane footprint of the spinel lattice (~ 0.8×0.8 nm^2), the fraction of distorted unit cells at the DB to the number of undistorted cells inside each phase is significant: about 30%, see Figure 6.10. Hence, these domain walls should also produce a significant contribution to the total diffraction picture. The DB diffraction signal can then be assigned to four additional diagonal streaks labeled ρ, σ, τ, and υ, in Figure 6.5. The angles between the DB have been determined from the angular separation between the ρ, σ, τ, and υ streaks in the H-K maps. The 90° angle between the υ–τ and ρ–σ streaks corresponds to domains with the twisted tetragonal phases, while the 97.5° and 82.5° separation of the ρ–τ, and σ–υ streaks confirms presence of the twined (perpendicularly oriented) diamond-shaped domains containing the orthorhombic phases. Note that the volume expansion for the orthorhombic phase (V/V_s = +0.013) is compensated by the volume decrease of the tetragonal phase (V/V_s = -0.022) thus minimizing the averaged volume change.

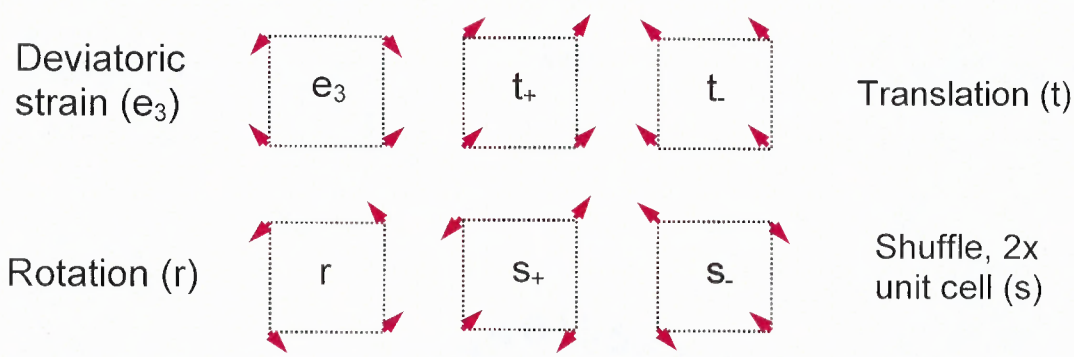

Figure 6.12 The in-plane CB pattern can be described in terms of these six distortion modes, which are with respect to a 2D square lattice. Six modes relevant to the CB pattern.

To better understand symmetry of the lattice distortions at the domain boundaries, it is useful to describe the in-plane CB pattern in terms of distortions with respect to a 2D square lattice. The mode-based atomic-scale description of the lattice distortions has recently been developed for a 2D square lattice with a monatomic basis [73,74]. Six modes relevant to the CB pattern are shown in Figure 6.12. Mode e_3 corresponds to square-to-rectangle distortions with a/b ratio $(1+e_3/\sqrt{2})/(1-e_3/\sqrt{2})$. If we represent $e_3 = \varepsilon > 0$ in the domain α, the domain δ, then has $e_3 = -\varepsilon$. Mode r represents rotations by an angle of $r/\sqrt{2}$ radian. The amplitude for the rotation mode is $r = \varepsilon$ in the γ domain and $r = -\varepsilon$ for the β domain. The distortions at the domain boundaries can be represented as a linear combination of e_3, r, and two other modes, either t_+ and s_+ or t_- and s_-. For example, distortions at the interface between the γ and δ domains, as illustrated in Figure 6.12, can be characterized by a combination of the $-e_3 + r + t_+ + s_+$ distortion modes with amplitudes of $e_3 = -\varepsilon/2$, $r = \varepsilon/2$, $t_+ = \varepsilon/2$, and $s_+ = \varepsilon/2$. Among these four modes, e_3 and r are strain modes, repetition of which can fill the entire space and shift the corresponding diffraction peak around the undisturbed RLP. In contrast, s_+ is a short wavelength (π, π) mode that should alternate its sign and double the unit cell to fill the entire space. Such short wavelength distortions could result in redistribution of the x-ray intensity between different reflection orders and could generate super-lattice peaks. Evidence of this can be seen by noting the stronger DB peaks from the (022) reflection in Figure 6.8 compared to those for the (044) reflection in Figure 6.5. Mode t_+ represents a rigid translation, the application of which does not change the x-ray diffraction pattern. Therefore, the distortions $e_3 = -\varepsilon/2$ and $r = \varepsilon/2$ within the DB could shift the diffraction peak from the undisturbed RLP position to the point right between the peaks from domain δ and domain

γ, which corresponds to peak τ, see Figures 6.5 and 6.8. If only scattering from a single domain interface is considered, the FWHM for DB peaks in the H-K plane should be very broad in the direction perpendicular to the boundary. The DB peaks, however are relatively narrow providing further experimental evidence for the highly coherent growth among neighboring domains in the CB structure. Note that this observation is in agreement with the aforementioned large value of the correlation length for all CB domains($D_{H-K} \approx 25\,\text{nm}$) that covers several identical DBs between the 4×4 nm^2 CB domains.

6.7 Conclusion

In conclusion the symmetry of atomic displacements at the domain boundaries provides the means for nearly dislocation-free coexistence of two types of domains in the volume of the film. In summary, the MgO substrate is covered by a thin elastically-strained $ZnGaMnO_4$ layer with no phase separation (peak *A*), where the relaxation process begins as evident in the tail of peak *A,* see Figure 6.6, between $\Delta L_A/L = 0.023$ and $\Delta L_{CB}/L = 0.017$. Eventually, accumulation of the volume strain energy results in partial relaxation of strain and formation of the elastically-strained CB layer consisting of two conversely rotated tetragonal and two orthogonal orthorhombic phases (α, β, γ, and δ). The corners of the CB super cell match perfectly to the MgO substrate, though influence from subgrain boundaries in the MgO substrate are not felt to be influential in the CB formation. The DBs, which are oriented along <110> and <1-10> directions, and separate orthorhombic and rotated tetragonal phases, accommodating the structural imparity between the α, β, γ, and δ phases by means of lattice distortions shown in Figure 6.13.

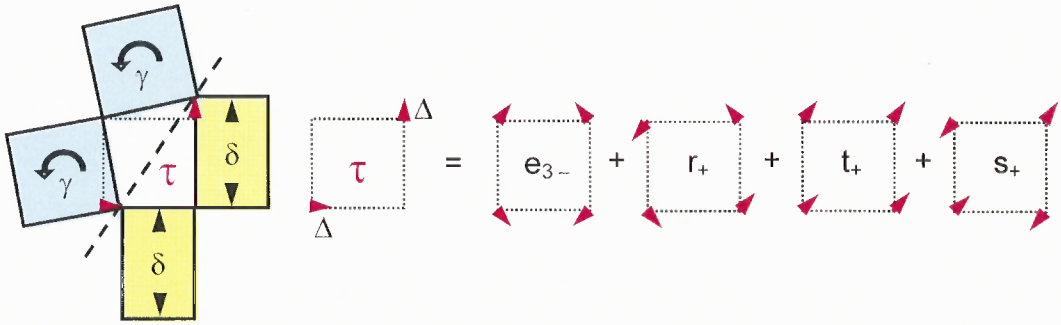

Figure 6.13 Representation of the linear combination of distortion modes at the domain boundary τ. Squares γ and rectangles δ correspond to the rotated tetragonal and orthorhombic lattices, respectively.

The accommodating mechanism is produced by contributions from the Mn^{3+} ions, which become JT-active upon occupying the octahedral sites in the spinel structure of the Mn-rich orthorhombic phase. The orbital degeneracy of the Mn ion ground state is lifted by structural distortions and the electric energy gain overcomes the cost of displacive structural energy.

Among open questions for the future theoretical analysis of the CB structures could be modeling of the exact in-plane size of the pattern and the mechanisms of suppression of the herring-bone structure for films *vs.* that in the bulk. The speculation is that the size of the CB domains is determined by various competing factors. The energy cost associated with the formation DBs would favor bigger domains since the number of the strained lattice cells at the DBs relative to the number of undisturbed cells decreases inversely proportional to the domain size. However, the domain size is limited from above by the diffusion length of Mn and Ga ions during the annealing, as indicated in a recent experiment on nano CB formation of a Mn-doped $CoFe_2O_4$ spinel compound [23]. Other factors, such as the strain energy cost between the CB film and the substrate would also influence the size of domains, giving rise to a nanometer length scale CB pattern and suppressed the herring-bone structure formation.

CHAPTER 7

CONCLUDING REMARKS

The usefulness of synchrotron light sources has proven itself important in the characterization of electronic and structural properties of novel material systems. In the case of this dissertation, the high-brightness and large flux densities of synchrotron radiation were utilized to characterize GaN-based device structures, nano-checkerboards films, and multiferroic crystals. To conclude this manuscript, a short summary of the key findings will follow.

Growth enhancement for GaN-based SAG structures with identical mask pattern and reactor conditions ought to have similar structural parameters under the law of source material conservation based on the gas phase diffusion of precursors towards the growth surface. The x-ray diffraction results, however clearly showed a differences in strain and growth enhancement between sample grown with orthogonal mash orientation. These differences indicate that other considerations must be taken into account, such as the exact ridge dimensions and inter-facet migration of group-III species. It was proposed that the difference in growth rates and strain dependence found between samples, is due to inter-facet migration effects, where the group-III species can migrate further on the {1-101} sidewall facet and contribute to growth on the top facet plane. In the case of sidewall MQW growth, the micro-beam XRD measures revealed an underlining GaN ridge containing a large tilt distortion of its lattice, which causes subsequent relaxation of the MQW strain near the ridge base. The period results showed a quasi-linear reduction width down the sidewall facet. The strong variation in growth rate was attributed to both

the relatively short diffusion length of the group-III precursors and inadequate intra-facet migration effects. The developed characterization technique will be useful for the future GaN-based integrated photonic structures.

Strong changes in the oscillator strength for low-frequency IR-excitations were observed in multiferroic crystals for light polarization along different crystalline axes at the magnetic commensurate-incommensurate transition $T_3 = 19$ K. Weaker changes in the IR excitation spectra at around $T_1 = 44$ K were followed by a slow decrease of absorption in the temperature range much higher than T_1 up to about 200 K. Infrared-active excitations at 10.5, 13, and 18 cm^{-1} were contributed to electric-dipole transitions between ligand-field states of R^{3+} ions. The change in the oscillator strength for low-energy IR excitations at T_3 is associated with modification of the wavefunction symmetry for the R^{3+} LF states, which is influenced by magnetic ordering of the Mn spin system. Additional neutron scattering experiment will still be required to prove the suggested existence of the collective LF-magnon excitations in multiferroics.

Reciprocal space mapping revealed the stain-accommodating interaction between the two phases of the CB structure for $ZnMnGaO_4$ thin films by lowering the volume strain energy and maintaining pinned to the MgO substrate. Among open questions for the future theoretical analysis of the CB structures is the modeling of the mechanisms that are responsible for suppression of the herring-bone structure in the epitaxial films.

REFERENCES

1. A. Kazimirov, D. H. Bilderback, R. Huang, A. Sirenko, and A. Ougazzaden, J. Phys. D: Appl. Phys. **37**, L9-L12 (2004).

2 F. Scholz, Prog. Crystal Growth and Charact. **35**, 243-262 (1997).

3 I. Vurgaftman, J. R. Meyer, and L. R. Ram-Mohan, J. Appl. Phys. **89**, 5815 (2001).

4 P. Gibart, Rep. Prog. Phys. **67**, 667-715 (2004).

5 S. Nakamura, M. Senoh, S. Nagahma, N. Iwasa, T. Yamada, T. Matsushita, H. Kiyoko, Y. Sugimoto, Jap. J. Appl. Phys. Lett. Part 2, **35**, L74-L76 (1996).

6 B. Neuert, Peter Bruckner, F. Habel, F. Scholz, *et. al.*, Appl. Phys. Lett. **87**, 182111 (2005).

7 A. Wakahara, T. Tokuda, X-Z Dang, S. Noda, and A. Sasaki, Appl. Phys. Lett. **71**, 906 (1997).

8 F. Bernardini, V. Fiorentini, and D. Vanderbilt, Phys. Rev. B **56**, R10024 (1997).

9 V. Fiorentini, F. Bernadini, F. Della Sala, A. Di Carlo, and P. Lugli, Phys. Rev. B **60**, 8849 (1999).

10 T. Takeuchi, H. Amano, and I. Akasaki, Jpn. J. Appl. Phys., Part 1 **39**, 413 (2000).

11 O. Amacher, J. Phys. D **31**, 2653 (1998).

12 L. S. Wang, S. Tripathy, Z. Wang, J. H. Teng, S. Y. Chow, and S. J. Chua, Appl. Phys. Lett. **89**, 011901 (2006).

13 H. Schmidt, Ferroelectrics **162**, 317-338 (1994).

14 T. Kimura, T. Goto, H. shintani, K. Ishizaka, T. Arima, and Y. Tokura, Nature **426**, 55 (2003).

15 N. Hur, S. Park, P.A. Sharma, S. Guha, and S-W. Cheong, Phys. Rev. Lett. **93**, 107207 (2004).

16 M. Fiebig, J. Phys. D: Appl. Phys. **38**, R123-R152 (2005).

17 N. A. Hill, J. Chem. B **104**, 6694 (2000).

18 V. E. Wood and A. Austin, Int. J. Magn. **5**, 303 (1973).

19 Correlated electron systems, Science, special issue, (2000).

20 S. Yeo, Y. Horibe, S. Mori, C. M. Tseng, C. H. Chen, A. G. Khachaturyan, C. L.Zhang, and S-W. Cheong, App. Phys. Lett. **89**, 233120 (2006).

21 B. S. Guiton and P. K. Davies, Nat. Mat. **6**, 586 (2007).

22 C. L, Zhang, S. Yeo, Y. Horibe, Y. J. Choi, S. Guha, M. Croft, S-W. Cheong, andS. Mori, Appl. Phys. Lett. **90**, 133123 (2007).

23 C. L. Zhang, C. M. Tseng, C. H. Chen, S. Yeo, Y. J. Choi, and S.-W. Cheong,Appl. Phys. Lett. **91**, 233110 (2007).

24 S. Park, Y. Horibe, T. Asada, L. S. Wielunski, N. Lee, P. L. Bonanno, S. M. O'Malley, A. A. Sirenko, A. Kazimirov, M. Tanimura, T. Gustafsson, and S-W. Cheong , Nano Lett. **8**, 720 (2008).

25 J. L. MacManus-Driscoll, P. Zerrer, H. Wang, H. Yang, J. Yoon, A. Fouchet, R. Yu, M. G. Blamire, and Q. X. Jia, Nat. Mat. **7**, 314 (2008).

26 H. Zheng, Q. Zhan, F. Zavaliche, M. Sherburne, F. Straub, M. P. Cruz, L.-Q. Chen, U. Dahmen, and R. Ramesh. Nano Lett. **6**, 1401 (2006).

27 P. F. Fewster, C.J. Curling, J. Appl. Phys. **62**, 10 (1987).

28 D. K. Bowen and B. K. Tanner, "High Resolution X-ray Diffractometry and Topography" Taylor and Francis, (2001).

29 G. Bauer, W. Richter, "Optical Characterization of Epitaxial Semiconductor Layers" Springer, (1996)

30 A. A. Sirenko, A. Kazimirov, R. Huang, D. H. Bilderback, S. O'Malley, V. Gupta, K. Bacher, L. J. P. Ketelsen, and A. Ougazzaden, J. Appl. Phys. **97**, 063512 (2005).

31 E. J. Mittemeijer and P. Scardi, "Diffraction Analysis of the microstructure of Materials", Springer (2004).

32 R. Chierchia, T. Bottcher, H. Heinke, S. Einfeidt, S. Figge and D. Hommel, J. Appl. Phys. **93**, 8918 (2003).

33 S.R. Lee, A. M. west, A. A. Allerman, K. E. Waldrip, D. M. Follstaedt, P. P. Provencio, D. D. Koleske, C. r. Aernathy, Appl. Phys. Lett. **86**, 241904 (2005).

34 R. Chierchia, T. Bottcher, S. Figge, M. Diesselberg, H. Heinke, D. Hommel, Phys. Stat. Sol. (b) **228**, No. 2, 403 (2001)

35 B. Heying, X. H. Wu, S. Keller, Y. Li, D. Kapolnek, B. P. Keller, S. P. DenBaars, J. S. Speck, Appl. Phys. Lett. **68**, 643 (1996)

36 P. F. Fewster, Rep. Prog. Phys. **59**, 1339-1407 (1996).

37 S. Pereira, M.R. Correia, E. Pereira, K.P. O'Donnell, E. Alves, A. D. Sequeira, N. Franco, I. M. Watson, C. J. Deatcher, Appl. Phys. Lett. **80**, 3913 (2002). Erratum: Appl. Phys. Lett. **81**, 3500 (2002).

38 A. Pimenov, A. A. Mukhin, V. Y. Ivanov, V. D. Travkin, A. M. Balbashov, and A. Loidl, Nature Physics **2**, 97 (2006).

39 J. Jackson, "Classical Electrodynamics", Wiley 2nd Ed. (1975).

40 V. Zelezny, E. Cockayne, J. Petzelt, M. F. Limonov, D. E. Usvyat, V. V. Lemanov, and A. A. Volkov, Phys. Rev. B **66**, 224303 (2002).

41 C. N. R. Rao, K. J. Rao, "Phase Transitions in Solids", McGram-Hill (1978).

42 G. H. Dieke, "Spectra and Energy Levels of Rare Earth Ions in Crystals" Wiley (1968).

43 A. Kazimirov, A. A. Sirenko, D. H. Bilderback, Z.-H. Cai, B. Lai, R. Huang, and A. Ougazzaden, J. Phys. D **38**, A50 (2005).

44 K. Nishizuka, M. Funato, Y. Kawakami, Sg. Fujita, Y. Narukawa, and T.Mukai, Appl. Phys. Lett. **85**, 3122 (2004).

45 M. A. Alam, R. People, Appl. Phys. Lett. **74**, 2617 (1999).

46 Y. J. Lee, et al., Thin Solid Films (2007), doi:10.1016/j.tsf.2006.12.016.

47 P. L. Bonanno, S. M. O'Malley, A. A. Sirenko, A. Kazimirov, Z.-H. Cai, T. Wunderer, P. Brückner, and F. Scholz, Appl. Phys. Lett., **92**, 123106 (2008).

48 P. Fini, H. Marchand, J. P. Ibbetson, S. P. DenBaars, U. K. Mishra, and J. S. Speck, J. Cryst. Growth **209**, 581 (2000).

49 M. E. Coltrin, C. C. Willan, M. E. Bartram, J. Han, N. Missert, M. H. Crawford, and A. G. Baca, MRS Internet J. Nitride Semicond. Res. **4S1**, G6.9 (1999).

50 N. Hur, S. Park, P. A. Sharma, J. S. Ahn, S. Guha, and S-W. Cheong, Nature **429**, 392 (2004).

51 C. R. dela Cruz, F. Yen, B. Lorenz, M. M. Gospodinov, C. W. Chu, W. Ratcliff, J. W. Linn, S. Park, and S-W. Cheong, Phys. Rev. B **73**, 100406(R) (2006).

52 S-W. Cheong and M. Mostovoy, Nature Materials **6**, 13-20 (2007).

53 B. Mihailova, M. M. Gospodinov, B. Güttler, F. Yen, A. P. Litvinchuk, and M. N. Iliev, Phys. Rev. B **71**, 172301 (2005).

54 A. F. García-Flores, E. Granado, H. Martinho, R. R. Urbano, C. Rettori, E. I. Golovenchits, V. A. Sanina, S. B. Oseroff, S. Park, and S.-W. Cheong, Phys. Rev. B **73**, 104411 (2006).

55 R. Valdés Aguilar, A. B. Sushkov, S. Park, S.-W. Cheong, and H. D. Drew, Phys. Rev. B **74**, 184404 (2006).

56 A. Pimenov, A. A. Mukhin, V. Y. Ivanov, V. D. Travkin, A. M. Balbashov, and A. Loidl, Nature Physics **2**, 97 (2006).

57 H. Katsura, A. V. Balatsky, and N. Nagaosa, Phys. Rev. Lett. **98**, 027203 (2007).

58 A. B. Sushkov, R. V. Aguilar, S. Park, S-W. Cheong, and H. D. Drew, Phys. Rev. Lett. **98,** 027202 (2007).

59 N. Hur, S. Park, P. A. Sharma, S. Guha, and S.-W. Cheong, Phys. Rev. Lett. **93**, 107207 (2004).

60 C. R. dela Cruz, F. Yen, B. Lorenz, S. Park, and S-W. Cheong, M. M. Gospodinov, W. Ratcliff, J. W. Linn, and C. W. Chu, J. Appl. Phys. **99**, 08R103 (2006).

61 A.A. Sirenko, C. Bernhard, A. Golnik, A. M. Clark, J. Hao, W. Si, and X. X. Xi, Nature **404**, 373 (2000).

62 N. W. Ashcroft and N. D. Mermin, "Solid State Physics", Holt, Rinehart and Winston (1976).

63 P.W. Anderson, Phys. Rev. **79**, 350 (1950).

64 S. Skanthakumar, C.-K. Loong, L. Soderholm, M. M. Abraham, and L. A. Boatner, Phys. Rev. B **51**, 12451 (1995).

65 O. P. Vajk, M. Kenzelmann, J.W. Lynn, S. B. Kim, and S.-W. Cheong, Phys. Rev. Lett. **94,** 087601 (2005).

66 G. R. Blake, L. C. Chapon, P. G. Radaelli, S. Park, N. Hur, S-W. Cheong, and J. Rodríguez-Carvajal, Phys. Rev. B **71**, 214402 (2005).

67 J. E. Lowther, J. Phys. C **7**, 4393 (1974).

68 J. J. Sakurai and R. L. Liboff, American Journal of Physics **54**, 668 (1986).

69 J. Koo, C. Song, S. Ji, J.-S. Lee, J. Park, T.-H. Jang, C.-H. Yang, J.-H. Park, Y. H. Jeong, K.-B. Lee, T. Y. Koo, Y. J. Park, J.-Y.Kim, D. Wermeille, A. I. Goldman, G. Srajer, S. Park, and S-W. Cheong, Phys. Rev. Lett. **99**, 197601 (2007).

70 Y. Ni, Y. M. Jin, and A. G. Khachaturyan, Acta Mat. **55**, 4903 (2007).

71 M. A. Ivanov, N. K. Tkachev, and A. Ya. Fishman, Low Temp. Phys. **25**, 459 (1999).

72 Y. Ni, and A. G. Khachaturyan, Acta Mat. **56**, 4498 (2008).

73 K. H. Ahn, T. Lookman, A. Saxena, and A. R. Bishop, Phys. Rev. B **68**, 092101 (2003).

74 J. Moon, T. F. Seman, and K. H. Ahn, arXiv:0707.1921.